NASA CONTRACTOR REPORT 166249

NASA-CR-166249
19820012270

Procedures for the Computation of Unsteady Transonic Flows Including Viscous Effects

Donald P. Rizzetta

CONTRACT NAS2-10762
January 1982

NASA

NASA CONTRACTOR REPORT 166249

Procedures for the Computation of Unsteady Transonic Flows Including Viscous Effects

Donald P. Rizzetta
Boeing Military Airplane Company
P.O. Box 3707
Seattle, WA 98124

Prepared for
Ames Research Center
under Contract NAS2-10762

National Aeronautics and
Space Administration

Ames Research Center
Moffett Field, California 94035

PROCEDURES FOR THE COMPUTATION OF UNSTEADY TRANSONIC FLOWS INCLUDING VISCOUS EFFECTS

ABSTRACT

Modifications of the code LTRAN2, developed by Ballhaus and Goorjian[1], which account for viscous effects in the computation of planar unsteady transonic flows are presented. Two models are considered and their theoretical development and numerical implemenation is discussed. Computational examples employing both models are compared with inviscid solutions and with experimental data. A description for use of the modified code is provided.

TABLE OF CONTENTS

I. INTRODUCTION

Solutions of planar inviscid unsteady transonic flowfields about thin airfoils are commonly obtained by time integration of the differential equation governing the velocity potential function. This method is particularly attractive because it permits the treatment of nonlinear flow phenomena including irregular shock wave motion. Development of the LTRAN2 code by Ballhaus and Goorjian[1] has made available an efficient time-implicit finite difference algorithm for obtaining solutions to the low-frequency small disturbance transonic potential equation. This code is currently employed for many unsteady applications and has evolved as a useful tool for performing aeroelastic calculations and flutter analysis.

While the inviscid flowfields computed by LTRAN2 provide a reasonable physical description for a wide range of unsteady flow conditions, these results are not adequate when viscous effects are significant. Such situations can involve complex flow structures characterized by the following phenomena:

1. Shock-boundary-layer interaction altering the shock strength and location,

2. Effective camber modification due to differences in the boundary-layer displacement on the upper and lower airfoil surfaces,

3. Displacement and camber effects of the near wake.

A detailed description of these effects can be provided through use of more exact equations governing the flow. It is not the purpose here to provide a complete description, but rather to account for viscous effects only as they impact upon the unsteady airfoil surface pressure distribution. The objective is to modify the basic LTRAN2 code in such a fashion that the aforementioned phenomena may be treated without seriously degrading efficiency. Inherent to this approach are several simplifying assumptions which are thought to prove adequate for aeroelastic applications.

It is postulated that the viscous boundary layer is in instantaneous equilibrium with the unsteady inviscid flow. A simple order of magnitude analysis indicates that this assumption is valid if the reduced frequency of the unsteady airfoil motion is small[2]. As a consequence, a steady form of the viscous modelling may be applied in a quasi-steady fashion.

The most complex aspect of viscous transonic flows is that of the shock-boundary-layer interaction. A number of calculations for both steady and unsteady flows [2,3] have indicated that this effect may be modelled by a simple computational artifice. This is accomplished by augmenting the surface geometry with a wedge-nosed ramp that is inserted at the base of the shock in an inviscid calculation.

The ramp weakens the strength of the shock, usually displacing it upstream from its inviscid location, thereby simulating the effects of boundary-layer displacement. The ramp angle is chosen such that an empirically defined post-shock pressure is recovered.

For many flows of interest, use of the ramp model alone will suffice to predict unsteady pressure distributions. When aft viscous effects are significant, the ramp is used in conjunction with an integral boundary-layer calculation over the rearward portion of the airfoil and the downstream wake. For this purpose "lag entrainment equations"[4,5] are employed, which have been found useful for the prediction of turbulent shear layers. In addition, a coupling of these equations with an inviscid algorithm has previously been used to compute steady transonic flowfields about airfoils, both with and without separated regions[6,7].

The sections that follow will first briefly review the theoretical development of the governing equations used to modify the LTRAN2 code. Numerical implementation and details of the modifications will be described. Finally, several computational examples will be presented and comparisons of the modified results will be made with inviscid solutions and with experiment.

II. THEORETICAL DEVELOPMENT

The basic unsteady small disturbance perturbation potential equation treated by LTRAN2 may be written as

$$\left(\frac{2kM_\infty^2}{\delta^{2/3}}\right)\phi_{xt} = \left[\left(\frac{1-M_\infty^2}{\delta^{2/3}}\right) - (\gamma+1)M_\infty^m\phi_x\right]\phi_{xx} + \phi_{yy} \qquad (1)$$

where $k = \omega c/U_\infty$ is the reduced frequency, γ the ratio of specific heats, M_∞ the freestream Mach number and subscripts denote partial differentiation. Here x and y are the streamwise and normal Cartesian coordinates normalized by c and $c\,\delta^{-1/3}$ respectively, where c is the airfoil chord and δ the thickness ratio. The time, t, has been normalized by ω^{-1}, ω being the circular oscillation frequency. The perturbation velocity potential function, ϕ, has been normalized by $cU_\infty\delta^{2/3}$ where U_∞ is the freestream velocity and m is commonly taken to be 2. If the airfoil surface is defined by $y^\pm = \delta^{2/3}f^\pm(x,t)$ the flow tangency condition may be expressed as

$$\phi_y^\pm = f_x^\pm \quad \text{on } y = 0^\pm \text{ for } 0 \le x \le 1 \; . \qquad (2)$$

Across the trailing vortex wake the contact conditions

$$\left[\phi_y\right] = 0 \qquad \text{(continuity of slope)} \qquad (3a)$$

$$\text{on } y = 0,\ x > 1$$

$$\left[\phi_x\right] = 0 \qquad \text{(continuity of pressure)} \qquad (3b)$$

are applied where the brackets denote the jump in the enclosed quantity from above to below the vortex sheet. At the outer boundaries the following conditions are applied:

$\phi = 0$ far upstream (4)

$\phi_y = 0$ far laterally (5)

$\phi_x = 0$ far downstream. (6)

Finally, the initial condition $\phi(x, y, 0) = I(x, y)$ is specified.

A. Viscous Ramp

The basis for development of the viscous ramp model is the observation in many steady experimental measurements that the post-shock pressure for turbulent flow over an airfoil corresponds approximately to that of the oblique shock produced by flow over a ramp with a wedge slope equal to the "detachment" angle[3]. This observation has proven extremely useful as a simple computational artifice which accounts for the gross dominant effects of the shock-boundary-layer interaction. Computational results generated by inviscid codes which have been modified to incorporate the ramp model have been shown to correlate well with experimental data in steady, and more recently unsteady calculations where the quasi-steady assumption has been invoked[2,8].

The geometry of the viscous ramp model is depicted schematically in Figure 1. It consists of a short precursor over which the surface slope varies from zero to the given wedge angle followed by the main ramp body along which the slope varies quadratically. At the ramp leading edge the ramp height and slope are continuous, and at the downstream end the slope and curvature vanish. The ramp is positioned with respect to the local instantaneous sonic point location and affinely scaled with the shock strength as determined by conditions immediately ahead of the shock. As was done in the steady case[3], the ramp leading edge is

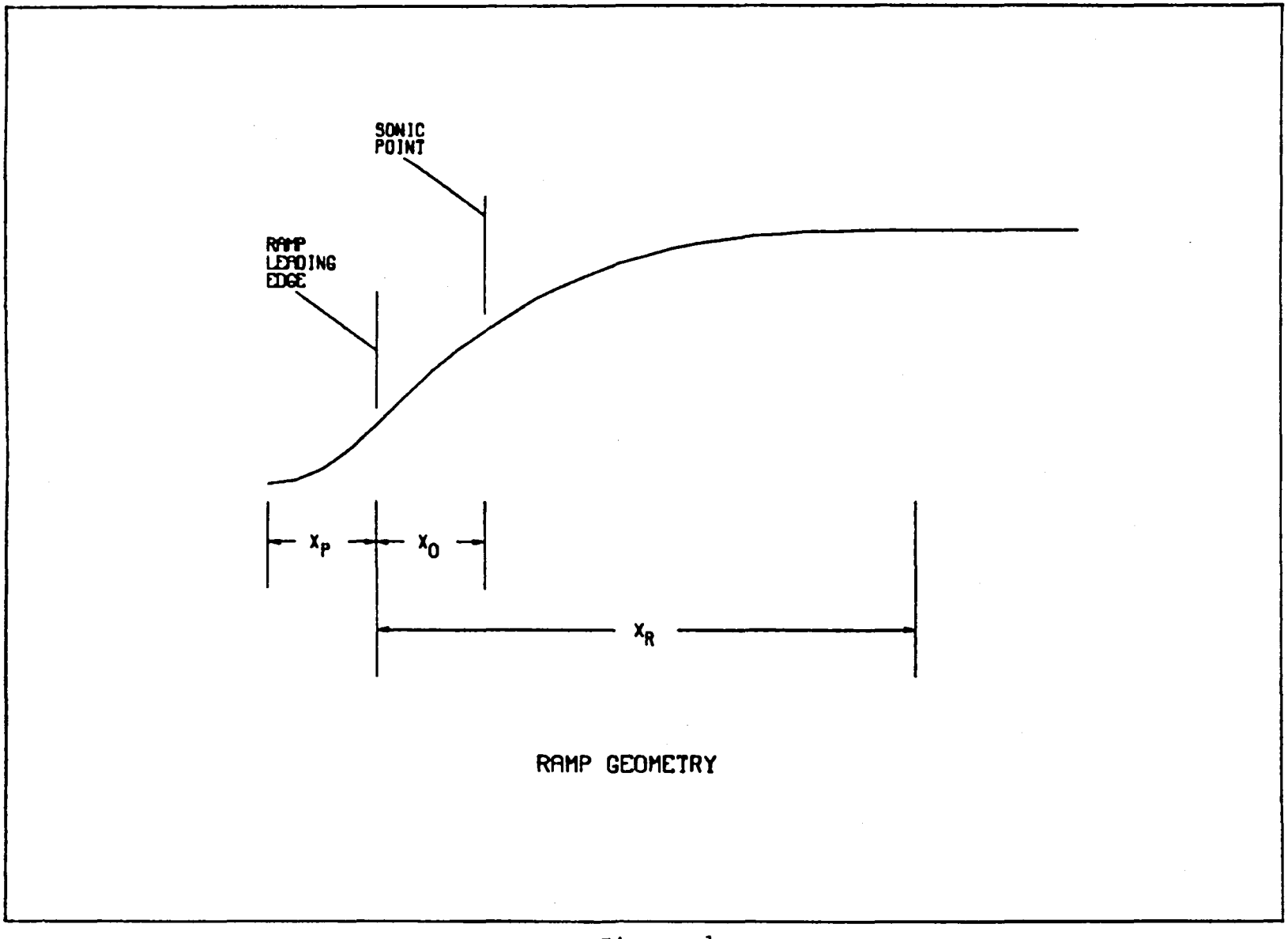

RAMP GEOMETRY

Figure 1.

offset a distance x_o ahead of the sonic location in order to more fully influence the numerical shock profile. The leading edge is preceded by the precursor of length x_p which has been used in previous unsteady calculations[2,8] to moderate the passage of the sharp ramp leading edge across computational mesh points, thereby precluding spurious numerical instabilities. The main body of the ramp has a length of x_R where the parameters x_p, x_o, and x_R may be selected for each specific application.

Augmenting the surface geometry by the ramp model results in the following modification to the tangency condition, Eq. 2:

$$\phi_y^{\pm} = f_x^{\pm} + f_{R_x}^{\pm} \quad \text{on } y = 0^{\pm} \text{ for } 0 \leq x \leq 1 \quad . \tag{7}$$

If x_s is the sonic point location and θ the wedge angle then $f_{R_x}^{\pm}$ is defined as follows:

$$f_{R_x}^{\pm} = 0 \text{ for } x < x_s - x_o - x_p \tag{8a}$$

$$f_{R_x}^{\pm} = \pm \left(\frac{\theta}{\delta}\right)\left[1 + \left(\frac{x - x_s + x_o}{x_p}\right)\right] \text{ for } x_s - x_o - x_p \leq x \leq x_s - x_o \tag{8b}$$

$$f_{R_x}^{\pm} = \pm \left(\frac{\theta}{\delta}\right)\left[1 - \left(\frac{x - x_s + x_o}{x_R}\right)^2\right] \text{ for } x_s - x_o \leq x \leq x_s - x_o + x_R \tag{8c}$$

$$f_{R_x}^{\pm} = 0 \text{ for } x > x_s - x_o + x_R \; . \tag{8d}$$

The instaneous wedge angle θ, corresponding to that for the maximum possible turning for an attached oblique shock is found from the following analysis. Consider a wedge of angle θ with an oblique shock located at its vertex. Within the approximations of small disturbance theory it is easily shown from the tangency condition that

$$\delta(\phi_{y2} - \phi_{y1}) = \tan\theta \approx \theta \tag{9}$$

where the subscripts 1 and 2 denote the upstream and downstream states respectively. We now write Eq. 1 in conservative form as

$$(a\,\phi_x)_t + (a\,\phi_t + b\,\phi_x + c\,\phi_x^2)_x + (\phi_y)_y = 0\ . \tag{10}$$

For convenience the following definitions have been made:

$$a = -\frac{k\,M_\infty^2}{\delta^{2/3}}\ ,\quad b = \frac{1 - M_\infty^2}{\delta^{2/3}}\ ,\quad c = -\frac{(\gamma + 1)M_\infty^2}{2}\ . \tag{11}$$

If $\vec{i}_t$, $\vec{i}_x$, and $\vec{i}_y$ are unit vectors in each of the coordinate directions, the following mass flux vector, $\vec{q}$, may be formed:

$$\vec{q} = (a\,\phi_x)\vec{i}_t + (a\,\phi_t + b\,\phi_x + c\,\phi_x^2)\vec{i}_x + (\phi_y)\vec{i}_y\ . \tag{12}$$

Given the unit vector normal to the shock, $\vec{n}$, the shock jump conditions are then defined by

$$[\vec{q}]\cdot\vec{n} = 0 \tag{13}$$

where $$[\ ] = (\ )_2 - (\ )_1\ .$$

Let us now assume that $h_s = x - g(y, t) = 0$ describes the shock geometry. It follows that $\vec{n}$ is equal to $\frac{\vec{\nabla} h_s}{|\vec{\nabla} h_s|}$.

Eq. 13 then becomes

$$- \left[a \phi_x\right] g_t + \left[a \phi_t + b \phi_x + c \phi_x^2\right] - \left[\phi_y\right] g_y = 0 \quad . \tag{14}$$

In a similar manner one may consider the jump conditions for the following relationships

$$(\phi_y)_x - (\phi_x)_y = 0 \tag{15a}$$

$$(\phi_x)_t - (\phi_t)_x = 0 \tag{15b}$$

and thereby eliminate the shock geometry, i.e., g_t and g_y. Upon so doing, one arrives at the "Rankine-Hugoniot" condition corresponding to Eq. 1:

$$2a(\phi_{t2} - \phi_{t1})(\phi_{x2} - \phi_{x1}) + b(\phi_{x2} - \phi_{x1})^2 \tag{16}$$

$$+ c(\phi_{x2} + \phi_{x1})(\phi_{x2} - \phi_{x1})^2 + (\phi_{y2} - \phi_{y1})^2 = 0 \ .$$

For maximum turning $\frac{\partial \phi_{y2}}{\partial \phi_{x2}} = 0$, a condition which is obtained from

Eq. 16 as

$$\phi_{x2} = -\frac{2b}{3c} - \frac{\phi_{x1}}{3} \tag{17}$$

using $\phi_{t2} - \phi_{t1} = 0$.

This relationship is now used in conjunction with Eq. 16 and Eq. 9 to find that

$$\frac{\theta}{\delta} = \pm \left[\frac{4}{(\gamma+1)M_\infty^m}\right]\left[\frac{(\gamma+1)M_\infty^m \phi_{x1} - \frac{(1-M_\infty^2)}{\delta^{2/3}}}{3}\right]^{3/2} . \tag{18}$$

Here the plus sign is taken for the upper surface and the minus sign for the lower surface.

B. Lag Entrainment Equations

The form of the so-called "lag entrainment equations" which will be considered here are those due to Green[9]. They are predicated upon the boundary-layer assumption that the normal extent of the viscous region is small when compared with airfoil or wake thickness, which necessarily applies to flows at high Reynolds numbers. By integrating the governing partial differential equations in the normal direction and suitably modelling the requisite relationships among the dependent variables, a system of three first order ordinary differential equations is obtained. Two of the equations result directly from continuity and momentum. The third evolves from the Bradshaw, Ferriss and Atwell[10] turbulent kinetic energy equation but is formulated in terms of the entrainment concept originally proposed by Head[11]. This yields a streamwise rate equation governing the degree to which the outer inviscid flow merges with the boundary layer.

The choice of an integral set of equations as opposed to a differential set is made for two reasons. First, integral techniques generally require considerably less computing time than differential methods. Second, differential methods have not as yet proven to be substantially superior for the computation of flows of practical interest. Since their original formulation the lag entrainment equations have proven to be a useful computational tool for performing compressible[4,9] and incompressible boundary-layer and wake calculations, involving both separated[5,7,12] and unseparated[6] flow regions.

For completeness, Green's lag entrainment integral equations are briefly summarized here. If a more thorough understanding of their development is required, the reader is referred to any of the original references[4,5,9]. It is useful to first note some preliminary definitions:

displacement thickness $$\delta^* = \int_0^\infty \left(1 - \frac{\rho U}{\rho_e U_e}\right) d\eta \qquad (19)$$

momentum defect thickness $$\theta = \int_0^\infty \frac{\rho U}{\rho_e U_e} \left(1 - \frac{U}{U_e}\right) d\eta \qquad (20)$$

shape factor $$H = \frac{\delta^*}{\theta} \qquad (21)$$

shape parameter $$\bar{H} = \frac{1}{\theta} \int_0^\infty \frac{\rho}{\rho_e} \left(1 - \frac{U}{U_e}\right) d\eta \, . \qquad (22)$$

entrainment coefficient $$C_E = \frac{1}{\rho_e U_e} \frac{d}{d\xi} \int_0^{\delta_{bl}} \rho U d\eta \, . \qquad (23)$$

In the preceding equations ξ and η are streamwise and normal physical coordinates respectively, ρ, the density and U the streamwise velocity component in the boundary layer. The subscript e refers to the boundary-layer edge denoted by $\eta = \delta_{bl}$. Within the confines of small disturbance theory and the boundary-layer limit, the edge conditions may be taken as those corresponding to the inviscid solution on the airfoil surface or the wake centerline.

The primary dependent variables are taken as θ, $\overline{H}$, and C_E. Given their value at any streamwise station, ξ, their distributions may be predicted by the following first order set of ordinary differential equations and subsequent parameters:

$$\frac{d\theta}{d\xi} = \frac{C_f}{2} - (H + 2 - M_e^2) \frac{\theta}{U_e} \frac{dU_e}{d\xi} \tag{24}$$

$$\frac{d\overline{H}}{d\xi} = \left(\frac{1}{\theta}\right) \frac{d\overline{H}}{dH_1} \left\{ C_E - H_1 \left[\frac{C_f}{2} - (H + 1) \frac{\theta}{U_e} \frac{dU_e}{d\xi} \right] \right\} \tag{25}$$

$$\frac{dC_E}{d\xi} = \left(\frac{F}{\theta}\right) \left\{ \left(\frac{2.8}{H+H_1}\right) \left[(C_\tau)_{EQO}^{1/2} - \lambda C_\tau^{1/2} \right] + \left(\frac{\theta}{U_e} \frac{dU_e}{d\xi}\right)_{EQ} \right.$$

$$\left. - \frac{\theta}{U_e} \frac{dU_e}{d\xi} \left[1 + 0.075 M_e^2 \frac{\left(1 + \frac{\gamma-1}{2} r M_e^2\right)}{1 + 0.1 M_e^2} \right] \right\} . \tag{26}$$

The following relationships are now used to complete the description of the governing equations:

$$F_c = \left[1 + \left(\frac{\gamma-1}{2}\right) r M_e^2 \right]^{1/2} , \tag{27}$$

$$F_R = 1 + 0.056\, M_e^2 , \tag{28}$$

$$Re_\theta = \frac{\rho_e U_e \theta}{\mu_e} , \tag{29}$$

$$C_{fo} = \frac{1}{F_c}\left[\frac{0.01013}{\log_{10}(F_R Re_\theta) - 1.02} - 0.00075\right] , \tag{30}$$

$$\frac{\overline{H}}{\overline{H}_o} = \overline{H}\left\{1 - 6.55\left[\left(\frac{C_{fo}}{2}\right)(1 + 0.04\, M_e^2)\right]^{1/2}\right\} , \tag{31}$$

$$C_f = \begin{cases} C_{fo}\ 0.9\left(\dfrac{\overline{H}}{\overline{H}_o} - 0.4\right)^{-1} - 0.05 & \text{for wall boundary layers} \\ 0 \text{ for wake shear layers,} \end{cases} \tag{32}$$

$$H = (\overline{H} + 1)\left[1 + \left(\frac{\gamma - 1}{2}\right) r M_e^2\right] - 1 , \tag{33}$$

$$H_1 = 3.15 + \left(\frac{1.72}{\overline{H} - 1}\right) - 0.01\,(\overline{H} - 1)^2 , \tag{34}$$

$$\frac{d\overline{H}}{d\overline{H}_1} = -\left[\frac{(\overline{H} - 1)^2}{1.72 + 0.02\,(\overline{H}+1)^3}\right] , \tag{35}$$

$$F = \frac{0.02\, C_E + C_E^2 + \dfrac{0.8\, C_{fo}}{3}}{0.01 + C_E} , \tag{36}$$

$$C_\tau = (1 + 0.1\ M_e^2)(0.024\ C_E + 1.2\ C_E^2 + 0.32\ C_{fo}) \ , \tag{37}$$

$$\lambda = \begin{cases} 1 & \text{for wall boundary layers where secondary influence of streamwise wall curvature have been neglected} \\ 1/2 & \text{for wake shear layers,} \end{cases} \tag{38}$$

$$\left(\frac{\theta}{U_e}\ \frac{dU_e}{d\xi}\right)_{EQ} = \left(\frac{1.25}{H}\right)\left[\frac{C_f}{2} - \left(\frac{\overline{H} - 1}{6.432\ \overline{H}}\right)^2 (1 + 0.04\ M_e^2)^{-1}\right], \tag{39}$$

$$(C_E)_{EQ0} = H_1\left[\frac{C_f}{2} - (H + 1)\left(\frac{\theta}{U_e}\ \frac{dU_e}{d\xi}\right)_{EQ}\right] \ , \tag{40}$$

$$(C_\tau)_{EQ0} = (1 + 0.1\ M_e^2)\Big\{ 0.024\ (C_E)_{EQ0} + 1.2\ \left[(C_E)_{EQ0}\right]^2 + 0.32\ C_{fo}\Big\}, \tag{41}$$

$$C = (C_\tau)_{EQ0}(1 + 0.1\ M_e^2)^{-1}\ \lambda^{-2} - 0.32\ C_{fo} \ , \tag{42}$$

$$(C_E)_{EQ} = \left(\frac{C}{1.2 + 0.0001}\right)^{1/2} - 0.01, \tag{43}$$

$$\left(\frac{\theta}{U_e}\ \frac{dU_e}{d\xi}\right)_{EQ} = \left[\frac{1}{H_1(H + 1)}\right]\left[\frac{H_1\ C_f}{2} - (C_E)_{EQ}\right] \ . \tag{44}$$

Using the small disturbance approximation, edge qualities may be written in terms of the inviscid solution as follows:

$$\frac{U_e}{U_\infty} = 1 + \delta^{2/3}\ \phi_x \ , \tag{45}$$

$$M_e = M_\infty \left\{ 1 + \left[1 + \left(\frac{\gamma - 1}{2}\right) M_\infty^2 \right] \delta^{2/3} \phi_x \right\} , \tag{46}$$

$$\frac{\rho_e}{\rho_\infty} = 1 - M_\infty^2 \, \delta^{2/3} \phi_x . \tag{47}$$

The pressure gradient parameter may be approximated as

$$\frac{1}{U_e} \frac{dU_e}{d\xi} = \frac{1}{c} \delta^{2/3} \phi_{xx} , \tag{48}$$

and the local Reynolds number based on momentum defect thickness by

$$Re_\theta = \left[\frac{\left(\frac{\rho_e}{\rho_\infty}\right) \left(1 + \delta^{2/3} \phi_x\right) \left(\frac{\theta}{c}\right)}{\left(\frac{\mu_e}{\mu_\infty}\right)} \right] R_{e_\infty} \tag{49}$$

where $R_{e_\infty} = \dfrac{\rho_\infty U_\infty c}{\mu_\infty}$

is the freestream Reynolds number based upon chord.

The viscosity ratio $\dfrac{\mu_e}{\mu_\infty}$ is now eliminated from Eq. (49) by noting that

$$\frac{T_e}{T_\infty} = 1 - (\gamma - 1) \delta^{2/3} M_\infty^2 \phi_x \tag{50}$$

and then employing the Sutherland viscosity law[13] in the form

$$\left(\frac{\mu_e}{\mu_\infty}\right) = \left(\frac{T_e}{T_\infty}\right)^{3/2} \left[\frac{1 + \frac{So}{T_\infty}}{\frac{T_e}{T_\infty} + \frac{So}{T_\infty}}\right] \tag{51}$$

where So is a constant dependent upon the nature of the specific gas (So = 110°K, for air). It is noted in Eq.'s 26, 27, and 33 that r is the recovery factor which is commonly chosen as a function of the turbulent Prandtl number Pr_t :

$$r = (Pr_t)^{1/3} \quad . \tag{52}$$

With these specifications the lag entrainment equations are fully defined. Noting that the shape parameter $\overline{H}$ and the entrainment coefficient C_E are already nondimensional, the equations are rewritten here in a form compatible with coupling to the inviscid solution:

$$\frac{d}{dx}\left(\frac{\theta}{c}\right) = \frac{C_f}{2} - (H + 2 - M_e^2)\,\delta^{2/3}\left(\frac{\theta}{c}\right)\phi_{xx} \,, \tag{53}$$

$$\frac{d\overline{H}}{dx} = \frac{1}{\left(\frac{\theta}{c}\right)}\frac{d\overline{H}}{dH_1}\left\{C_E - H_1\left[\frac{C_f}{2} - (H + 1)\,\delta^{2/3}\left(\frac{\theta}{c}\right)\phi_{xx}\right]\right\}, \tag{54}$$

$$\frac{dC_E}{dx} = \frac{F}{\left(\frac{\theta}{c}\right)}\left\{\left(\frac{2.8}{H + H_1}\right)\left[(C_\tau)_{EQO}^{1/2} - \lambda C_\tau^{1/2}\right] + \left(\frac{\theta}{Ue}\frac{dU_e}{d\xi}\right)_{EQ}\right.$$

$$- \delta^{2/3} \left(\frac{\theta}{c}\right) \phi_{xx} \left[1 + 0.075\, M_e^2 \frac{\left(1 + \frac{\gamma-1}{2} r\, M_e^2\right)}{1 + 0.1\, M_e^2}\right]\Bigg\}. \qquad (55)$$

Given initial values of $\left(\frac{\theta}{c}\right)$, $\overline{H}$, and C_E at the streamwise station $x = x_i$, Eq.'s 53 through 55 may be integrated in the downstream direction for all $x > x_i$ to obtain the distribution of viscous parameters along the airfoil surface and trailing wake.

These are then used to modify the inviscid solution through use of the displacement thickness, δ^*. An explicit dependence of the slope of the displacement thickness, $\frac{d\delta^*}{d\xi}$ upon the viscous parameters provided by the lag entrainment equations may be obtained by the following analysis. From Eq. 21 we write

$$\frac{d\delta^*}{d\xi} = H \frac{d\theta}{d\xi} + \theta \frac{dH}{d\xi} \quad . \qquad (56)$$

Differentiating Eq. 33 results in the expression

$$\frac{dH}{d\xi} = \left[1 + \left(\frac{\gamma-1}{2}\right) r\, M_e^2\right] \frac{d\overline{H}}{d\xi} + (\gamma-1)\, r\, Me\, (\overline{H} + 1) \frac{dMe}{d\xi} . \qquad (57)$$

Now, using the isentropic relationship[13]

$$\frac{U_e}{a_o} = Me \left[1 + \left(\frac{\gamma-1}{2}\right) M_e^2\right]^{-1/2} \qquad (58)$$

where a_o is the speed of sound at the stagnation condition, it may be shown that

$$\frac{dMe}{d\xi} = M_e \left[1 + \left(\frac{\gamma-1}{2}\right) M_e^2\right] \left(\frac{1}{U_e} \frac{dU_e}{d\xi}\right) . \qquad (59)$$

Upon substitution of Eq. 59 into Eq. 57 to obtain

$$\frac{dH}{d\xi} = \left[1 + \left(\frac{\gamma-1}{2}\right) r\, M_e^2\right] \frac{d\bar{H}}{d\xi}$$

$$+ \ (\gamma-1) r\, M_e^2\, (\bar{H}+1) \left[1 + \left(\frac{\gamma-1}{2}\right) M_e^2\right] \left(\frac{1}{Ue} \frac{dU_e}{d\xi}\right) , \qquad (60)$$

and subsequent use of Eq. 60 in conjunction with Eq. 56 results in

$$\frac{d\delta^*}{d\xi} = H\frac{d\theta}{d\xi} + \theta \left\{ \left[1 + \left(\frac{\gamma-1}{2}\right) r\, M_e^2 \right] \frac{d\bar{H}}{d\xi} \right.$$

$$\left. + (\gamma-1)\, r\, M_e^2\, (\bar{H}+1) \left[1 + \left(\frac{\gamma-1}{2}\right) M_e^2\right] \left(\frac{1}{Ue} \frac{dUe}{d\xi}\right)\right\} . \qquad (61)$$

Finally, the derivatives on the right-hand side of Eq. 61 are eliminated by employing Eq.'s 24 and 25 to arrive at

$$\frac{d\delta^*}{d\xi} = \frac{H C_f}{2} + \left[1 + \left(\frac{\gamma-1}{2}\right) r\, M_e^2\right] \left(C_E - \frac{H C_f}{2}\right)$$

$$+ \left\{ \left[1 + \left(\frac{\gamma-1}{2}\right) r\, M_e^2 \right] H_1 (H+1) \frac{d\bar{H}}{dH_1} \right.$$

$$\left. + (\gamma-1) r\, M_e^2\, (\bar{H}+1)\right] - H\,(H+2 - M_e^2)\} \left(\frac{\theta}{Ue} \frac{dUe}{d\xi}\right) . \qquad (62)$$

By nondimensionalizing Eq. 62 and applying the small disturbance assumption, we can transform this relationship to a form compatible with the inviscid equation as

$$\frac{d}{dx}\left(\frac{\delta^*}{\delta c}\right) = F_1 + F_2\,\phi_{xx} \tag{63}$$

where for convenience we have defined

$$F_1 = \left\{ \frac{H C_f}{2} + \left[1 + \left(\frac{\gamma-1}{2}\right) r\, M_e^2\right]\left(C_E - \frac{H C_f}{2}\right)\right\} \delta^{-1}, \tag{64a}$$

$$F_2 = \left\{ \left[1 + \left(\frac{\gamma-1}{2}\right) r\, M_e^2\right]\left[H_1\,(H+1)\,\frac{d\bar{H}}{dH_1} + (\gamma-1) r\, M_e^2\,(\bar{H}+1)\right]\right. \tag{64b}$$

$$\left. - H\,(H+2-M_e^2)\right\}\ \delta^{-1/3}\ \left(\frac{\theta}{c}\right).$$

The form of Eq. 63 was first inferred by East[5] et. al. who noted several interesting properties. For unseparated flows, $\left|F_2\,\phi_{xx}\right| << \left|F_1\right|$ so that Eq. 63 represents a stiff equation for $\frac{d}{dx}\left(\frac{\delta^*}{\delta c}\right)$. Thus, the displacement is relatively insensitive to the pressure gradient, ϕ_{xx}. On the other hand, for fully separated flows $\left|F_2\right| >> \left|F_1\right|$. In this case Eq. 63 may be rewritten as

$$\phi_{xx} = \left[\frac{d}{dx}\left(\frac{\delta^*}{\delta c}\right) - F_1\right] F_2^{-1},$$

which is a stiff equation for ϕ_{xx}. Eq. 63 is now used to provide the coupling between the inviscid and viscous solutions. The original

surface boundary condition, Eq. 2, is modified by the viscous displacement thickness to yield

$$\phi_y^{\pm} = f_x^{\pm} + \left(\frac{\delta^*}{\delta c}\right)_x^{\pm} \quad \text{on} \quad y = o^{\pm} \quad \text{for } o \leq x \leq 1. \tag{65}$$

Using Eq. 63 this is written as

$$\phi_y^{\pm} = f_x^{\pm} + (F_1 + F_2\, \phi_{xx})^{\pm} \text{ on } y = 0^{\pm} \text{ for } 0 \leq x \leq 1 \tag{66}$$

in order to exhibit the dominant explicit dependence of the displacement upon the velocity potential.

Downstream of the trailing edge, the viscous wake generates an effective displacement afterbody. Due to its presence, a discontinuity in the slope of the potential is now permitted such that the wake condition Eq. 3a must be replaced by

$$\left[\phi_y\right] = \left[F_1 + F_2\, \phi_{xx}\right] \quad \text{on } y = 0 \quad \text{for } x > 1\ . \tag{67}$$

III. NUMERICAL METHOD

A. Viscous Ramp

Given the velocity potential distribution $\phi(x, y, t^n)$ over the computational domain at time level t^n, the viscous ramp model is implemented in the following manner in order to extend the solution to time level $t^{n+1} = t^n + \Delta t$. First, the sonic point, x_s, defined as that location where the surface pressure attains the critical value (C_p^*), is located based upon $\phi(x, y, t^n)$. A simple linear interpolation between mesh points is employed for this purpose. Next, the condition ϕ_{x1} is evaluated where the upstream location is taken to be that position which lies two mesh points upstream of the first subsonic point. The first subsonic point is that mesh point immediately downstream of x_s. With ϕ_{x1} now known, the value of the ramp angle is calculated from Eq. 18. Given this value and the sonic point location, the ramp geometry is computed according to Eq. 8. Finally, the modified boundary condition, Eq. 7, may be applied and the solution advanced to the new time level t^{n+1}.

The ramp geometric parameters x_p, x_o, and x_R can be adjusted for specific applications to provide desired computational results. This is often a matter of trial and error and it is suggested that comparisons with steady experimental pressure distributions, if available, be used for this purpose. The modified LTRAN2 code will accept these variables as input parameters. In addition, the following program default values have been proven adequate for a wide range of both steady and unsteady calculations:

$$x_p = 0.02,$$
$$x_o = 0.02,$$
$$x_R = 0.10.$$

B. Lag Entrainment Equations

The coupling of the lag entrainment equations with an inviscid solution algorithm can be an especially sensitive procedure. This is particularly true in the transonic regime where it is in general necessary to integrate the integral equations through the numerical shock profile. The transition from supersonic to subsonic flow regions can often produce numerical oscillations, instabilities, or other anomalous behavior. In addition, the structure of the shock profile is typically determined by the numerical techniques of the shock capturing method rather than a strict modelling of the physical processes involved. For example, the use of backward and centered streamwise differencing in the supersonic and subsonic regions respectively generally produces a shock profile with a streamwise extent of two mesh intervals. Thus the nature of the solution in this region is very much dependent upon the mesh distribution unless it is exceedingly fine. Although these deficiencies are not serious enough to degrade the accuracy of the results for aeroelastic applications, any rigorous coupling of the viscous and inviscid solutions through the shock profile is necessarily superfluous.

For these reasons, use of the viscous ramp model is maintained in conjunction with the lag entrainment equations. As was done previously, it is assumed that the solution $\phi(x, y, t^n)$ at time level t^n is known over the entire computational domain. It is consistent with the quasi-steady assumption, then, to use this solution to integrate the lag entrainment equations and extend the potential distribution to the next time level $t^{n+1} = t^n + \Delta t$. An initial upstream position, x_i, is selected as a location ahead of the shock. It is assumed that upstream of x_i the effect of the boundary layer will be negligible.

Initial values for the quantities $(\frac{\theta}{c})$, $\overline{H}$, and C_E at station x_i are obtained from empirical correlations for the incompressible turbulent boundary layer on a flat plate[14]. In particular, we assume

$$\frac{\delta^*}{c} = 0.04625\ x^{4/5}\ Re_\infty^{-1/5} \quad . \tag{68}$$

Then using the relationship

$$\frac{U}{Ue} = (\frac{n}{\delta_{b1}})^{1/7} \tag{69}$$

and Eq.'s 19 through 23 we can find that

$$\frac{\theta}{c} = (\frac{7}{9})\ (\frac{\delta^*}{c}) \ , \tag{70}$$

$$\overline{H} = \frac{(\frac{\delta^*}{c})}{(\frac{\theta}{c})} \ , \tag{71}$$

$$C_E = 7\ \frac{d}{dx}\ (\frac{\delta^*}{c}) \quad . \tag{72}$$

With the initial conditions specified, the parameters So, Re_∞, T_∞, and Pr_t defined, and the distribution $\phi(x, y, t^n)$ given, Eqs. 53 through 55 may be integrated from the station $x = x_i + \Delta x$ to the downstream boundary. For this purpose a second order accurate Runge-Kutta predictor-corrector numerical integration scheme was employed. While other more accurate techniques could easily have been selected, the truncation error incurred in the chosen method is of the same order as that of the inviscid algorithm. The evaluation of the expressions in Eqs. 45 thorugh 49 was performed using a central

difference to calculate ϕ_x and either a central or backward difference to compute ϕ_{xx} based upon the local flow characteristics (i.e., a central difference was used in subsonic regions and a backward difference was used in supersonic regions). This treatment is not only consistent with the inviscid algorithm, but also duplicates the technique employed in previous steady computations[6,7]. Once the integration has been completed the functions F_1 and F_2 defined in Eq. 64 may be evaluated along the airfoil surface and entire trailing viscous wake. These are then employed to couple the viscous soluion to the inviscid solution through the use of Eqs. 66 and 67.

Although integration of the lag entrainment equations is initiated upstream of the shock, coupling with the inviscid flow does not occur until the first mesh point downstream of the shock for which the flow is locally subsonic, defined as x_{sub}. This ensures that the turbulent variables have properly adjusted to the shock-boundary-layer interaction when the coupling procedure is invoked. Upstream of x_{sub}, the viscous ramp technique is implemented in the fashion described in the previous section. Beginning at x_{sub}, Eq. 66 is used as the modified boundary condition for the inviscid solution. This treatment can potentially produce anomalous behavior due to inconsistencies between the respective methods, but none have been observed and the procedure appears to be reasonably stable numerically.

Equation 66 is approximated by evaluating ϕ_y as a first order one-sided difference and ϕ_{xx} as a second-order central difference, as the condition is only applied in subsonic flow regions. If it is assumed that the solution at the new time level t^{n+1} has been generated for all $x < x_I$, then Eq. 66 for the upper surface may be expressed at $x = x_I$ as follows:

$$\left(\frac{\phi^{n+1}_{I,\,JW+1} - \phi^{n+1}_{I,\,JW}}{Y_{JW+1} - Y_{JW}}\right) = f_{XI} + F_{1I}$$

$$+ F_{2I}\left[\frac{\left(\frac{\phi^{n}_{I+1,\,JW} - \phi^{n+1}_{I,\,JW}}{X_{I+1} - X_{I}}\right) - \left(\frac{\phi^{n+1}_{I,\,JW} - \phi^{n+1}_{I-1,\,JW}}{X_{I} - X_{I-1}}\right)}{\left(\frac{X_{I+1} - X_{I-1}}{2}\right)}\right] \qquad (73)$$

where $y_{JW} = 0^{+}$. It is noted that at the station just downstream of the station under consideration, X_{I+1}, a value for ϕ at the previous time level must be taken in order that the inviscid algorithm remain intact. Equation 73 is now rearranged such that all known quantities appear on the right-hand side:

$$\left(\frac{1}{Y_{JW+1} - Y_{JW}}\right) \phi^{n+1}_{I,\,JW+1}$$

$$+\left[\left(\frac{2F_{2I}}{X_{I+1} - X_{I-1}}\right)\left(\frac{1}{X_{I+1} - X_{I}} + \frac{1}{X_{I} - X_{I-1}}\right) - \frac{1}{Y_{JW+1} - Y_{JW}}\right] \phi^{n+1}_{I,\,JW}$$

$$= f_{XI} + F_{1I} + \left(\frac{2F_{2I}}{X_{I+1} - X_{I-1}}\right)\left(\frac{\phi^{n}_{I+1,\,JW}}{X_{I+1} - X_{I}} + \frac{\phi^{n+1}_{I-1,\,JW}}{X_{I} - X_{I-1}}\right) . \qquad (74)$$

When used in conjunction with the difference expressions for the flowfield differential equation, this relationship provides an implicit expression simultaneously coupling all points above the airfoil ($y \geq 0^{+}$) at the station x_I. This treatment is considered to be significant in suppressing numerical instabilities which would otherwise occur, particularly in regions of large pressure gradient such as those at the trailing edge. An expression similar to Eq. 74 may easily be obtained for the lower surface.

Downstream of the trailing edge, the effects of the viscous wake are manifested in the jump condition, Eq. 67. This impacts upon the inviscid algorithm through the term ϕ_{yy} in the governing differential equation when evaluated along $y = 0$ for $x > 1$. It follows from Eq. 36 that once the jump in potential at the trailing edge is found at time level t^{n+1}, it is uniquely determined for all subsequent downstream stations. Thus ϕ_{yy} may be evaluated along either $y = 0^+$ or $y = 0^-$ and the value along the opposite side of the wake determined from Eq. 36.

We now consider $(\phi_{yy})_{I,\,JW}$ where $y_{JW} = 0^-$ and $x > 1$ and for convenience define

$$\Gamma_I^{n+1} = \phi\,(X_I,\, 0^+,\, t^{n+1}) - \phi\,(X_I,\, 0^-,\, t^{n+1})\,, \tag{75}$$

$$\beta_I = \phi_y\,(X_I,\, 0^+,\, t^{n+1}) - \phi_y\,(X_I,\, 0^-,\, t^{n+1})\,. \tag{76}$$

Using Eq. 67, we can express Eq. 76 as

$$\beta_I = (F_{1I}^+ - F_{1I}^-) + (F_{2I}^+\ \phi_{xxI}^+ - F_{2I}^-\ \phi_{xxI}^-)\,. \tag{77}$$

Because the wake is entirely subsonic, a central difference is used to approximate the derivatives in Eq. 77 such that

$$\beta_I = (F_{1I}^+ - F_{1I}^-) + F_{2I}^+ \left[\frac{\left(\frac{\phi_{I+1}^+ - \phi_I^+}{X_{I+1} - X_I}\right) - \left(\frac{\phi_I^+ - \phi_{I-1}^+}{X_I - X_{I-1}}\right)}{\left(\frac{X_{I+1} - X_{I-1}}{2}\right)}\right]$$

$$- F_{2I}^- \left[\frac{\left(\frac{\phi_{I+1}^- - \phi_I^-}{X_{I+1} - X_I}\right) - \left(\frac{\phi_I^- - \phi_{I-1}^-}{X_I - X_{I-1}}\right)}{\left(\frac{X_{I+1} - X_{I-1}}{2}\right)}\right]. \tag{78}$$

Values of the potential on the upper side of the wake are now eliminated through use of Eq. 75. In addition, we note that the potential at the upstream station X_{I-1} at the new time level are known, those at the current station X_I are to be solved for, and those at the downstream station X_{I+1} must be taken at the previous time level t^n. Thus we may write

$$\beta_I^{n+1} = \left(\frac{2}{X_{I+1} - X_{I-1}}\right)\left(\frac{1}{X_{I+1} - X_I} + \frac{1}{X_I - X_{I-1}}\right)(F_{2I}^- - F_{2I}^+)\underline{\phi}_I^{n+1}$$

$$+ (F_{1I}^+ - F_{1I}^-) + \left(\frac{2}{X_{I+1} - X_{I-1}}\right)\left\{\left[\left(\frac{\overset{n}{\overset{+}{\phi}}_{I+1}}{X_{I+1} - X_I}\right)\right.\right.$$

$$- \left(\frac{1}{X_{I+1} - X_{I-1}} + \frac{1}{X_I - X_{I-1}}\right) \Gamma_I^{n+1}$$

$$\left.\left. + \left(\frac{\Gamma_{I-1}^{n+1} + \underline{\phi}_{I-1}^{n+1}}{X_{I+1} - X_I}\right)\right] F_{2I}^+ - \left[\left(\frac{\underline{\phi}_{I+1}^{n}}{X_{I-1} + X_I}\right) + \left(\frac{\underline{\phi}_{I-1}^{n+1}}{X_I - X_{I-1}}\right)\right] F_{2I}^-\right\}. \quad (79)$$

A second order approximation for $(\phi_{yy})_{I,\,JW}$ may now be written as

$$(\phi_{yy})_{I,\,JW} = \frac{\left(\frac{\tilde{\phi}_{I,\,JW+1} - \phi_{I,\,JW}}{Y_{JW+1} - Y_{JW}}\right) - \left(\frac{\phi_{I,\,JW} - \phi_{I,\,JW-1}}{Y_{JW} - Y_{JW-1}}\right)}{\left(\frac{Y_{JW+1} - Y_{JW-1}}{2}\right)}, \quad (80)$$

where $\tilde{\phi}_{I,\,JW+1}$ is a modified value of $\phi(X_I,\, Y_{JW+1})$.

Because ϕ and ϕ_y are discontinuous on $y = 0$, the value of $\tilde{\phi}_{I,\,JW+1}$ must be computed in terms of $\phi_{I,\,JW+1}$, Γ_I, and β_I. From a Taylor series expansion about $y = 0^-$, we write

$$\tilde{\phi}_{I,JW+1} = \phi_{I,\,JW} + (Y_{JW+1} - Y_{JW})\,\phi^-_{YI} + O\left[(Y_{JW+1} - Y_{JW})^2\right]. \quad (81)$$

Similarly, expanding about $y = 0+$,

$$\phi_{I,JW+1} = \phi^+_I + (Y_{JW+1} - Y_{JW})\,\phi^+_{YI} + O\left[(Y_{JW+1} - Y_{JW})^2\right]. \quad (82)$$

Upon combining Eqs. 81 and 82 along with Eqs. 75 and 76, the following expression is obtained:

$$\tilde{\phi}_{I,\,JW+1} = \phi_{I,\,JW+1} - \Gamma_I - (Y_{JW+1} - Y_{JW})\,\beta_I . \quad (83)$$

Finally, Eq. 83 is substituted into Eq. 80, the resultant expression evaluated at time level $n + 1$ and $\beta_I^{\,n+1}$ eliminated by use of Eq. 79 to arrive at the expression

$$\begin{aligned}
(\phi_{YY})^{n+1}_{I,\,JW} = {} & \left(\frac{2}{Y_{JW+1} - Y_{JW-1}}\right)\left(\frac{1}{Y_{JW+1} - Y_{JW}}\right)\phi^{n+1}_{I,\,JW+1} \\
& - \left(\frac{2}{Y_{JW+1} - Y_{JW-1}}\right)\left[\left(\frac{1}{Y_{JW+1} - Y_{JW}} + \frac{1}{Y_{JW} - Y_{JW-1}}\right)\right. \\
& \left. + \left(\frac{2}{X_{I+1} - X_{I-1}}\right)\left(\frac{1}{X_{I-1} - X_I} + \frac{1}{X_I - X_{I-1}}\right)\left(F^-_{2I} - F^+_{2I}\right)\right]\phi^{n+1}_{I,\,JW} \\
& + \left(\frac{2}{Y_{JW+1} - Y_{JW-1}}\right)\left(\frac{1}{Y_{JW+1} - Y_{JW}}\right)\phi^{n+1}_{I,\,JW-1}
\end{aligned}$$

$$- \left(\frac{2}{Y_{JW+1} - Y_{JW-1}}\right) \left(F^{+}_{1I} - F^{-}_{1I}\right)$$

$$- \left(\frac{2}{Y_{JW+1} - Y_{JW-1}}\right) \left(\frac{2}{X_{I+1} - X_{I-1}}\right) \left\{ \left[\left(\frac{\overset{n}{\overset{+}{\phi}}_{I+1}}{X_{I+1} - X_I} \right) \right.\right.$$

$$- \left(\frac{1}{X_{I+1} - X_I} + \frac{1}{X_I - X_{I-1}}\right) \Gamma_I^{n+1}$$

$$\left.\left. + \left(\frac{\Gamma^{n+1}_{I-1} + \phi^{n+1}_{I-1,JW}}{X_{I+1} - X_I} \right) \right] F^{+}_{2I} - \left[\left(\frac{\phi^{n}_{I+1,JW}}{X_{I+1} - X_I} \right) + \left(\frac{\phi^{n+1}_{I-1,JW}}{X_I - X_{I-1}} \right) \right] F^{-}_{2I} \right\}$$

$$- \left(\frac{2}{Y_{JW+1} - Y_{JW-1}}\right) \left(\frac{\Gamma_I^{n+1}}{Y_{JW+1} - Y_{JW}}\right) \quad . \tag{84}$$

Equation 84 now provides the implicit condition coupling the inviscid algorithm with the viscous downstream wake.

IV. COMPUTED RESULTS

In order to validate the modifications to the LTRAN2 code and to establish the acceptability of generated solutions, several computational examples of practical interest were considered. Two airfoil sections were selected as being representative of those for which viscous effects may be significant, namely the RAE 2822 and the NLR 7301. Section geometries are shown in Figure 2. The RAE 2822 section has a maximum thickness to chord ratio of 0.1210 and is characterized by appreciable camber, but a thin nose region. On the other hand, the NLR 7301 section has a very thick blunt leading edge, a large aft cove, and a thickness ratio of 0.1683. These sections, particularly the NLR 7301, are considered to be a severe test of the limitations inherent in the computational method. This selection is based upon the existence of experimental data available for comparative purposes[15,16].

All of the results presented here were generated on a nonuniform Cartesian grid consisting of 113 points in the x-direction and 97 points in the y-direction, symmetric about $y = 0$. Minimum grid spacings were $\Delta x_{min} = 0.005$ at the leading edge, $\Delta y_{min} = 0.01$ at the surface, and the computational domain was defined by

$$-200 \leq x \leq 200,$$
$$-397.8 \leq y \leq 397.8.$$

The airfoil surface was defined by 48 points in the x-direction. For each of the cases considered, results were generated for an inviscid solution, the viscous ramp solution, and the lag entrainment solution. Comparisons between these results, and with experiment when available, were then made.

A. The RAE 2822 Airfoil

Solutions for the steady flow at $M_\infty = 0.73$, $\alpha = 3.19^0$, and $Re_\infty = 6.5 \times 10^6$ over the RAE 2822 section were obtained by integrating in time. The inviscid solution was evolved from an initial

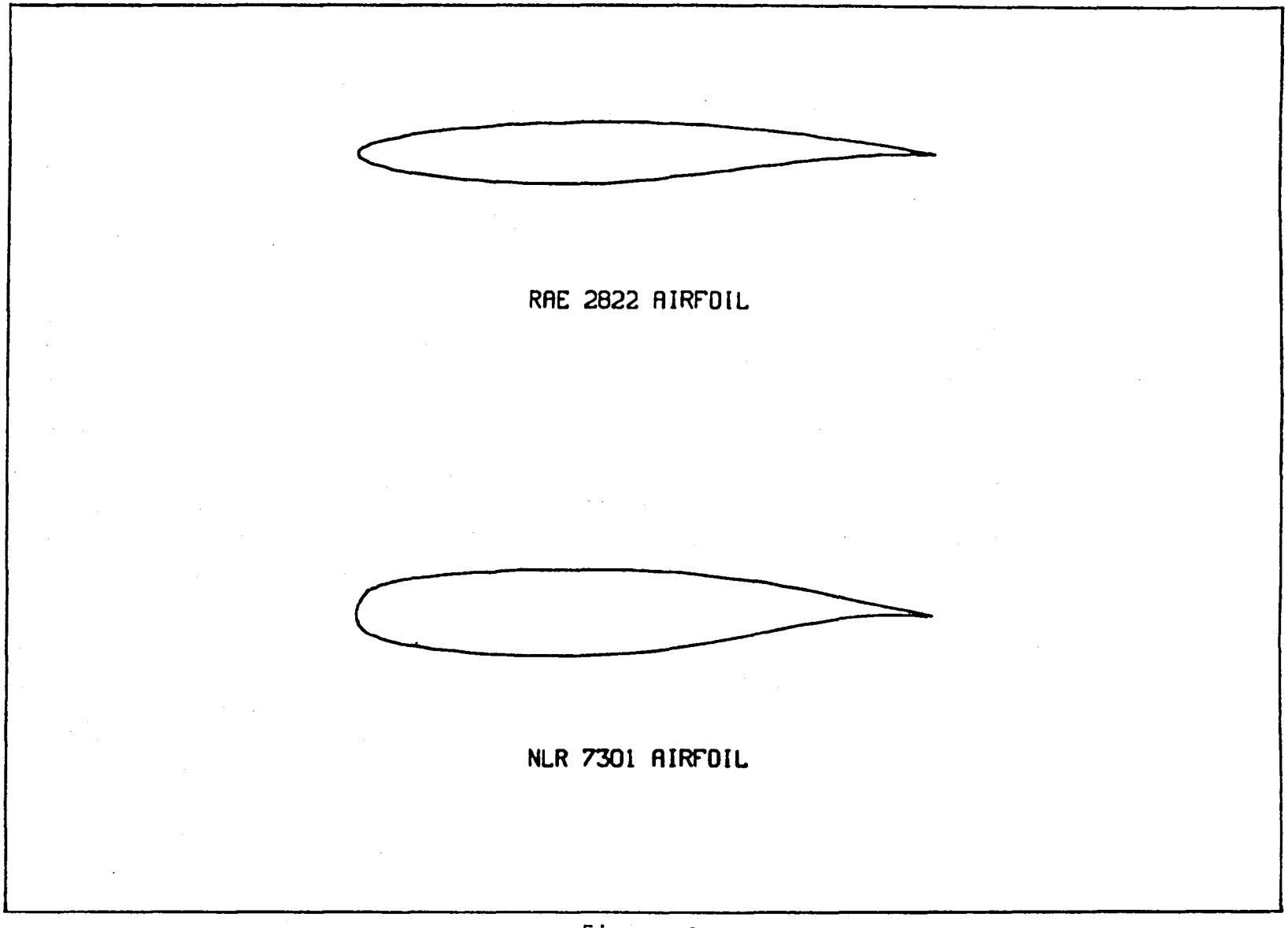

Figure 2.

undistributed flow (i.e., $\phi = 0$). This result was then used as the initial flow to obtain the viscous ramp solution, which in turn provided the initial condition for the lag entrainment result. While this process may not in general be optimal, it was employed here because all three solutions were required for comparison, and has been used to generate all subsequent steady results. Implementation of either the viscous ramp or lag entrainment computation (which is used in conjunction with the ramp) usually requires a local minimum of the pressure occurring over the airfoil surface in order to initiate the computation. This provides a starting location upstream of the trailing edge for the viscous effects to impact upon the solution as was noted in earlier formulations for steady solutions obtained by relaxation[3].

Surface pressure distributions for this case appear in Figure 3 and are compared with the experimental results of Cook[15] et al. It is seen that the inviscid shock location lies downstream of the experimental position. The inclusion of viscous effects displaces the shock forward. Location of the shock appears to be predicted quite well by use of the wedge alone, but not by the lag entrainment solution. The reason for this is that this case is particularly sensitive to small perturbations in the flow conditions. Other computations[17], for example, have slightly varied the Mach number and angle of attack to obtain better agreement with the experiment. Just upstream and downstream of the shock it is noted that the lag entrainment solution produces a pressure distribution that has no appreciable gradient. This evidences the fact that the shock position has little perferred location and will be quite sensitive to small perturbations in the flow conditions. The lag entrainment solution is also seen to produce better agreement with experiment upstream of the shock, on the lower surface, and in the trailing edge region. In this result the viscous displacement has properly accounted for the effective decambering of the airfoil. Because this effect is absent in the wedge solution, its close agreement with the experimenal shock location may be fortuitous.

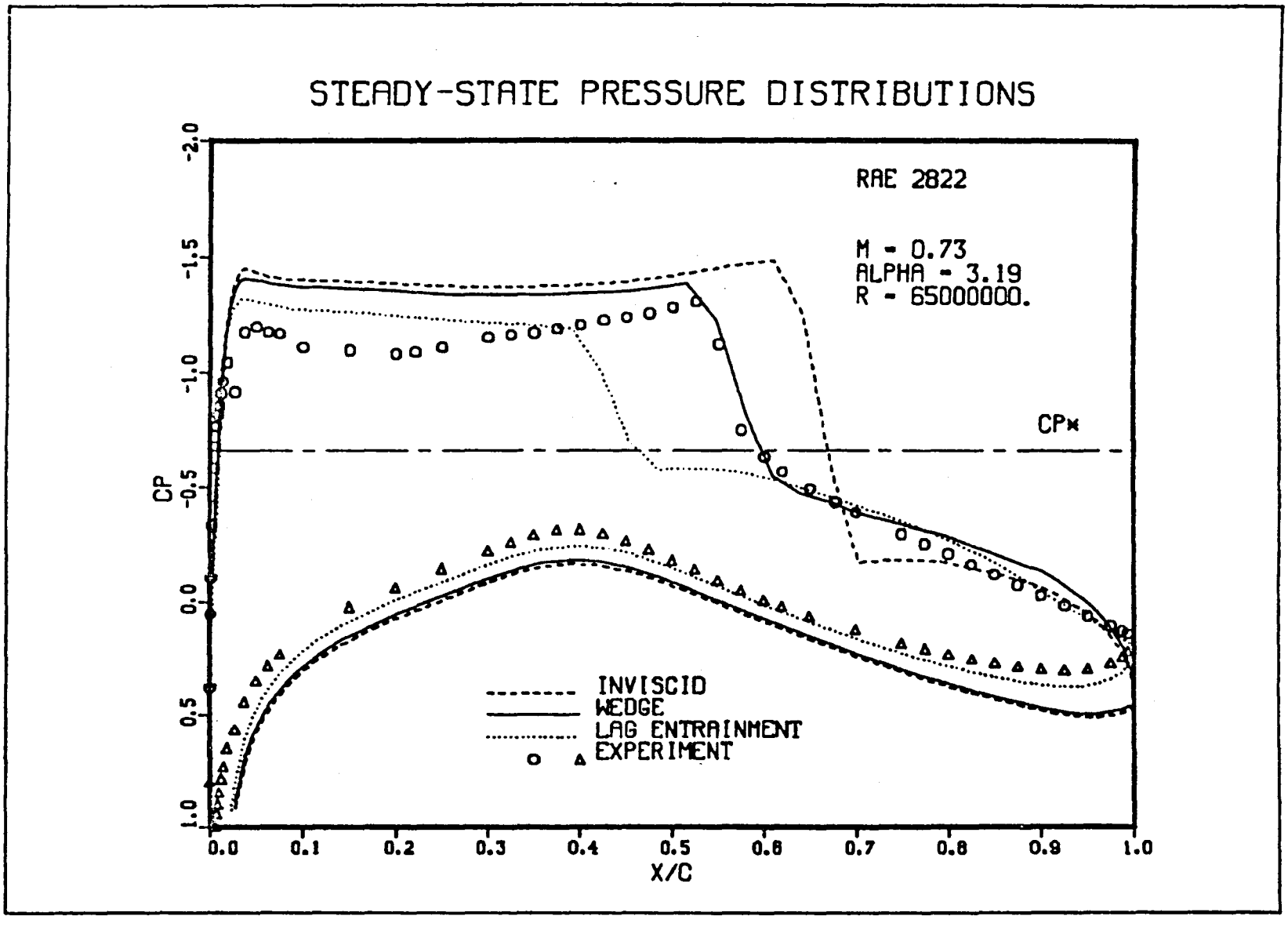
STEADY-STATE PRESSURE DISTRIBUTIONS
RAE 2822
M = 0.73
ALPHA = 3.19
R = 65000000.
CPx
CP
X/C
INVISCID
WEDGE
LAG ENTRAINMENT
EXPERIMENT
-2.0
-1.5
-1.0
-0.5
0.0
0.5
1.0
0.0
0.1
0.2
0.3
0.4
0.5
0.6
0.7
0.8
0.9
1.0

Figure 3.

Distributions of the upper surface displacement thickness and momentum defect thickness corresponding to this case appear in Figure 4. The comparison of the computed solutions with experiment is qualitatively correct. Downstream of the shock, the levels of the computation lie somewhat below the experiment. This is probably because the shock location is poorly predicted. If the shock were located further aft, the rise of θ and δ^* through the shock would be expected to be greater due to a larger local Reynolds number in the wake region. In addition, the behavior may be due in part to the fact that the inviscid and viscous solutions are not coupled through the shock profile. Downstream of the trailing edge θ and δ^* can be seen approaching a constant value which is consistent for free shear layers without pressure gradient. This is indicated, for example, in Eq. 53 with $C_f = \phi_{xx} = 0$.

In order to exemplify the sensitivity of this computation to the flow conditions, a second solution was generated for $M_\infty = 0.75$. Pressure distributions for this case are shown in Figure 5. Upon comparing this result with those in Figure 3 for $M_\infty = 0.73$, it can be seen that the slight increase in Mach number has produced a significant effect on the numerical solutions. It is observed in the inviscid computation that the shock has moved to the trailing edge and that in the wedge solution, the shock location is far aft of the experimental position. The lag entrainment result, on the other hand, compares quite well with the data and appears to duplicate a previous steady calculation[7]. Once again, the reason for this is because the lag entrainment solution accounts for the aft displacement effects, while the other results do not. This effect is also noticeable on the lower surface and in the regions both ahead of the shock and at the trailing edge. The anomalous behavior of the wedge result just upstream and downstream of the shock probably is produced by the positioning of the wedge within the shock profile. This behavior could possibly be eliminated by alternate choices for the wedge parameters (x_p, x_0, x_R), but no attempt was made to do that here.

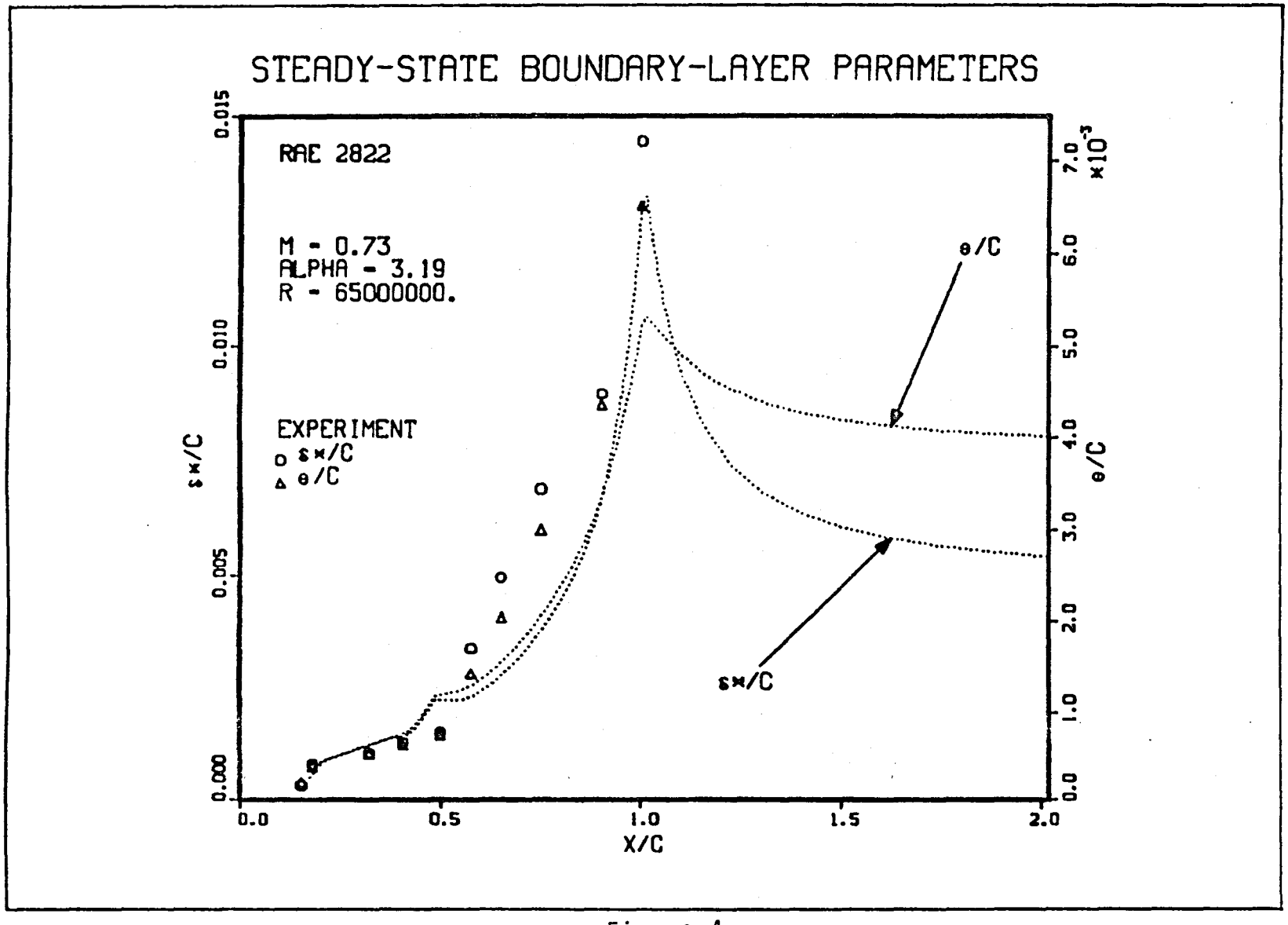
STEADY-STATE BOUNDARY-LAYER PARAMETERS
RAE 2822
M = 0.73
ALPHA = 3.19
R = 65000000.
EXPERIMENT
δ*/C
θ/C
θ/C
δ*/C
δ*/C
θ/C
X/C
0.000
0.005
0.010
0.015
0.0
0.5
1.0
1.5
2.0
1.0
2.0
3.0
4.0
5.0
6.0
7.0
×10⁻³

Figure 4.

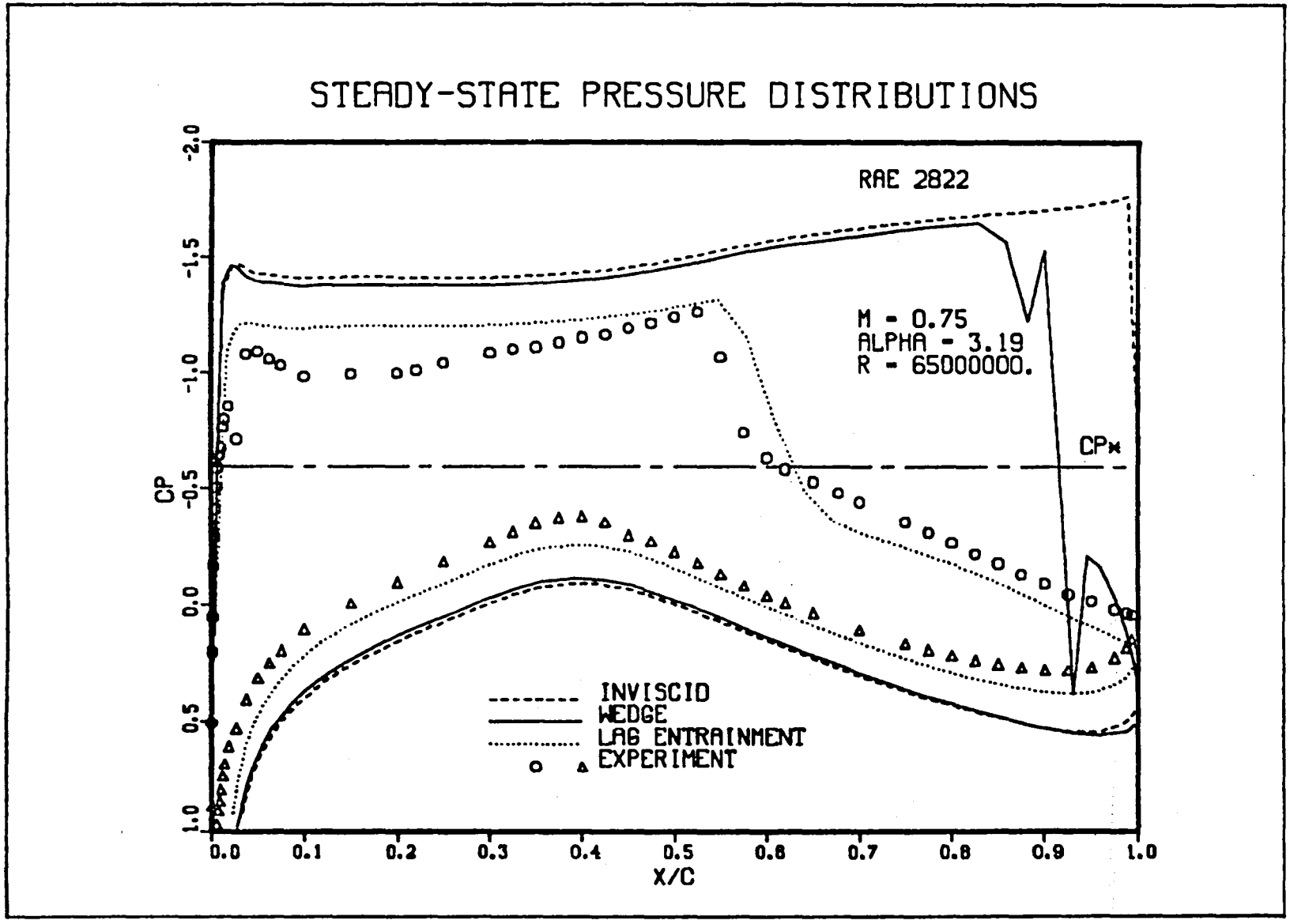
STEADY-STATE PRESSURE DISTRIBUTIONS
RAE 2822
M = 0.75
ALPHA = 3.19
R = 65000000.
CP*
CP
X/C
INVISCID
WEDGE
LAG ENTRAINMENT
EXPERIMENT
-2.0
-1.5
-1.0
-0.5
0.0
0.5
1.0
0.0
0.1
0.2
0.3
0.4
0.5
0.6
0.7
0.8
0.9
1.0

Figure 5.

Corresponding upper surface distributions of the boundary layer quantities are presented in Figure 6. The lack of agreement with the data occurs because the flow was found to separate experimentally, but remained attached for the computed solution. Much higher levels in θ and δ^* naturally occur downstream of separation. This condition is once again probably quite sensitive to the flow conditions. It is interesting to note that the numerical results of Reference 7 overpredicted the level of the δ^* distribution, while those presented here have underpredicted it. The fact that the pressure distributions of both results compare well with experiment is due to the fact that the coupling between the inviscid and viscous solutions is provided by $\frac{d\delta^*}{dx}$ which is insensitive to ϕ_{xx} as was noted earlier.

As an example of an unsteady calculation, this airfoil was forced to oscillate sinusoidally in rotation about the mid-chord at $M_\infty = 0.73$ with a reduced frequency $k = 0.2$ and an amplitude of 1^0, The solution was initiated from the steady-state results in Figure 3 and the oscillation was allowed to proceed for three cycles with Δt selected such that 0.5^0 of rotation occurred in one time step. Figure 7 shows the instantaneous surface pressure distributions for the last cycle of oscillation where the time is referenced to the beginning of this cycle and given in degrees. The inviscid result for this case could not be computed with the same time step, and thus does not appear in the comparison.

As was noted in the steady pressure distributions, the lag entrainment solution produces a weaker shock with more forward displacement than occurs for the wedge alone. Also, the effects of decambering on the lower surface and in the trailing edge region are noticeable. At $t = 360$ the wedge is seen to generate a post shock re-expansion. Use of the viscous ramp can cause this behavior which may be altered by variation of the ramp parameters.

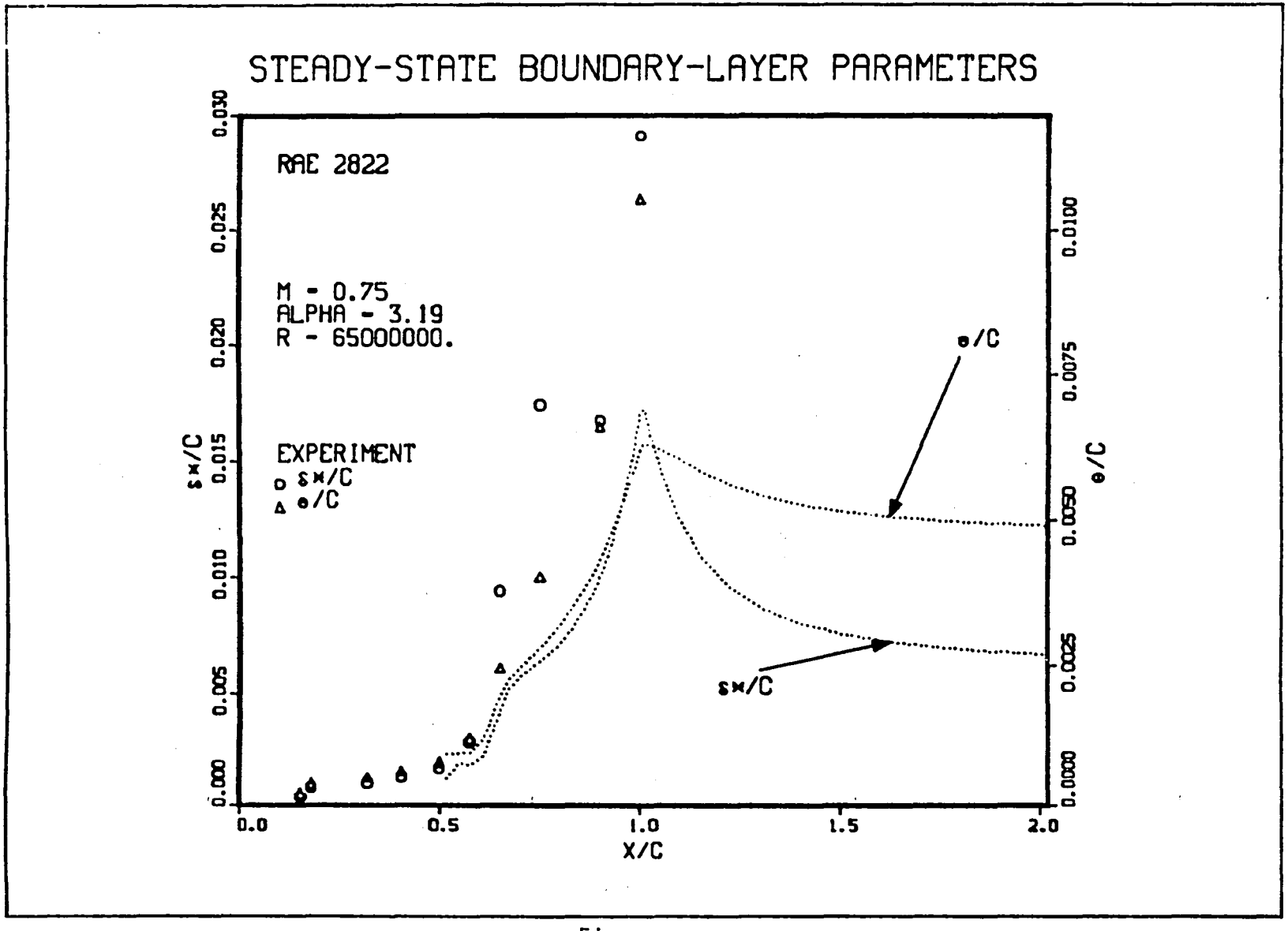
STEADY-STATE BOUNDARY-LAYER PARAMETERS
RAE 2822
M - 0.75
ALPHA - 3.19
R - 65000000.
EXPERIMENT
o δ*/C
Δ θ/C
θ/C
δ*/C
δ*/C
θ/C
X/C
0.000
0.005
0.010
0.015
0.020
0.025
0.030
0.0000
0.0025
0.0050
0.0075
0.0100
0.0
0.5
1.0
1.5
2.0

Figure 6.

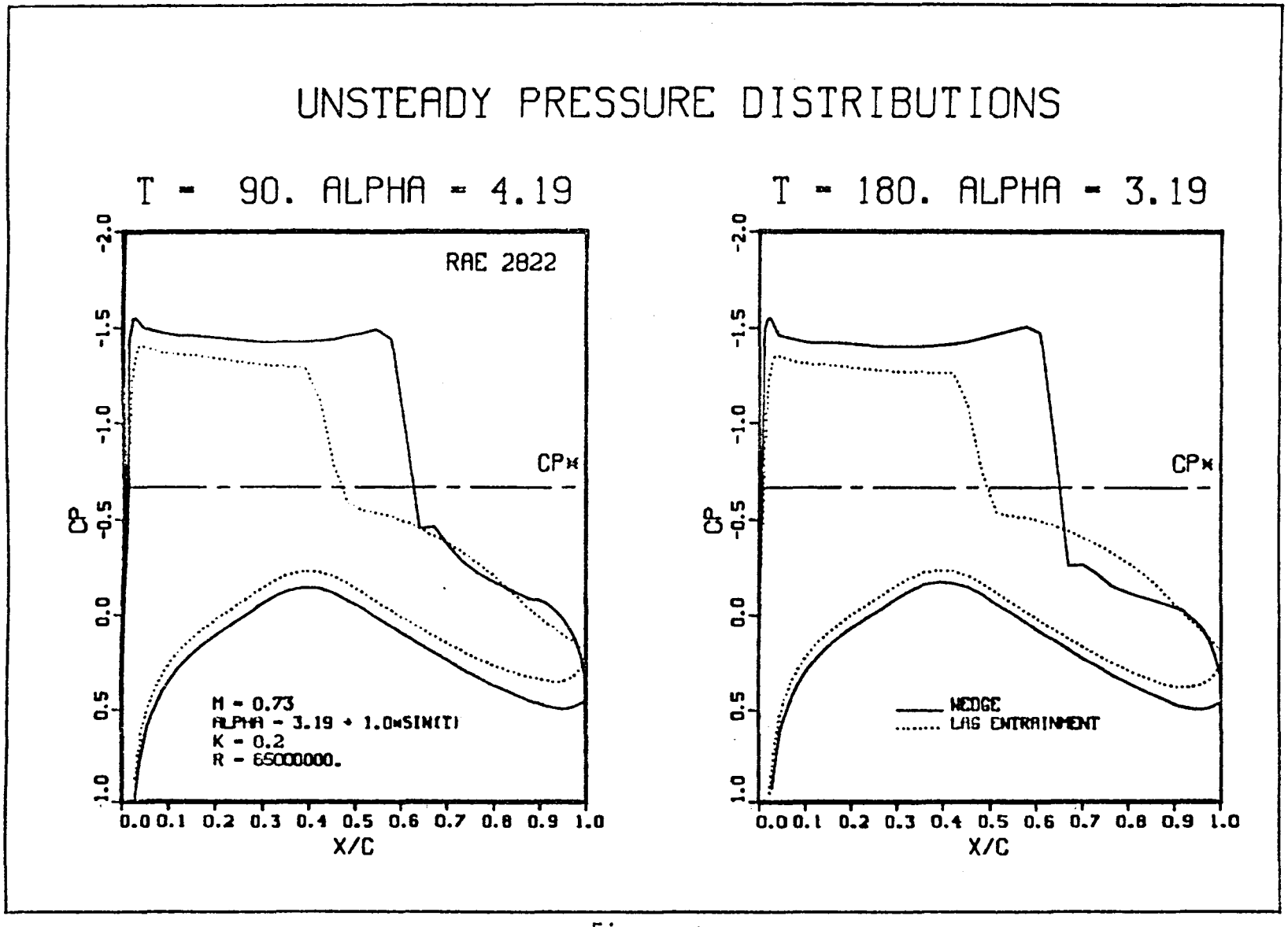
UNSTEADY PRESSURE DISTRIBUTIONS
T = 90. ALPHA = 4.19
RAE 2822
CP*
M = 0.73
ALPHA = 3.19 + 1.0*SIN(T)
K = 0.2
R = 65000000.
CP
X/C
T = 180. ALPHA = 3.19
CP*
WEDGE
LAG ENTRAINMENT
CP
X/C

Figure 7a.

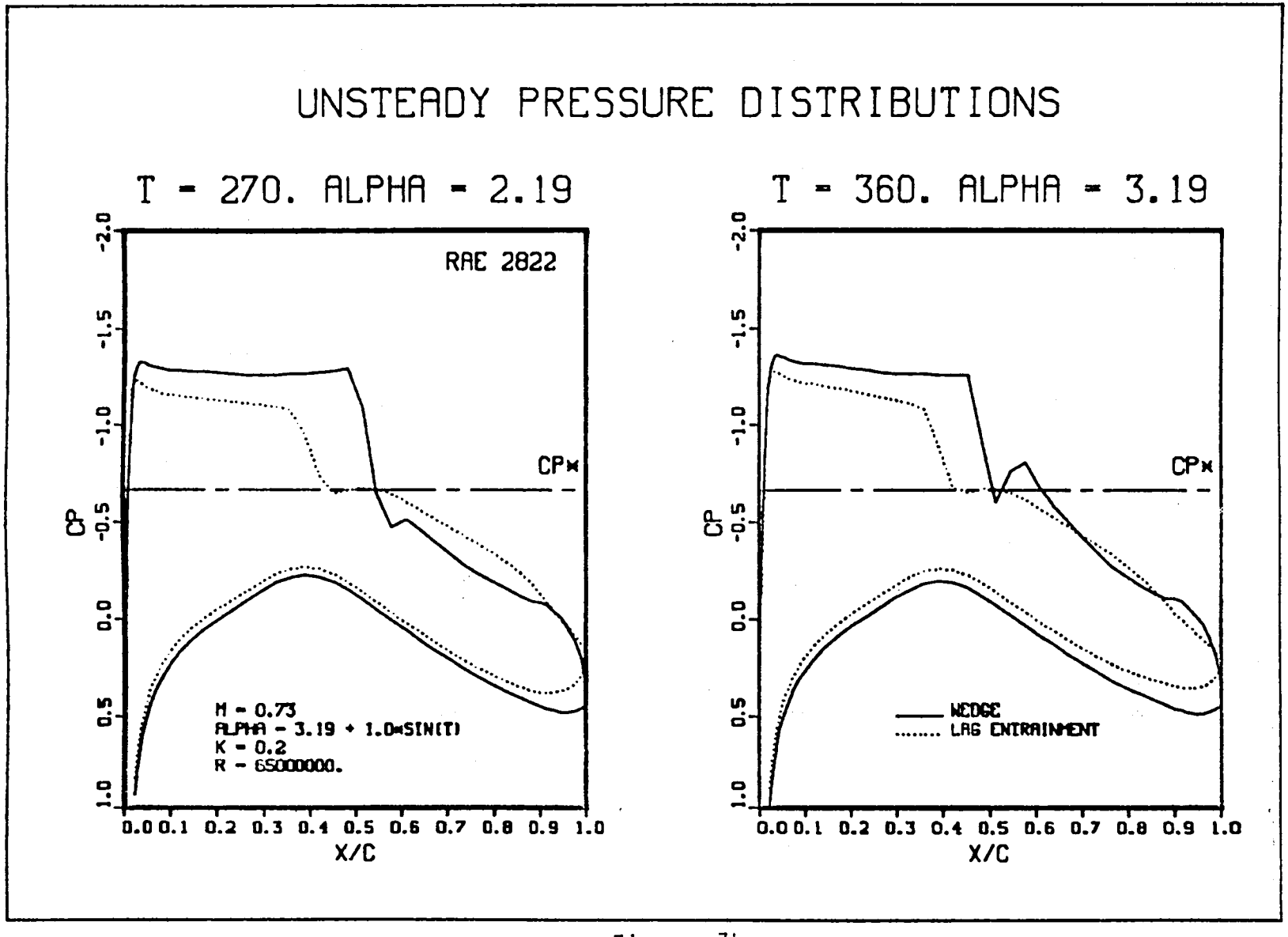
UNSTEADY PRESSURE DISTRIBUTIONS
T = 270. ALPHA = 2.19
RAE 2822
CP*
M = 0.73
ALPHA = 3.19 + 1.0*SIN(T)
K = 0.2
R = 65000000.
CP
-2.0
-1.5
-1.0
-0.5
0.0
0.5
1.0
0.0 0.1 0.2 0.3 0.4 0.5 0.6 0.7 0.8 0.9 1.0
X/C
T = 360. ALPHA = 3.19
CP*
WEDGE
LAG ENTRAINMENT
CP
X/C

Figure 7b.

Instantaneous upper surface distributons of the displacement and momentum defect thickness for this case appear in Figure 8. They exhibit the same general properties of the steady-state results (Figure 4). In Figure 9 the time histories of the unsteady lift and moment coefficients are presented. Here the moment coefficient is taken about the pitch point x = 0.5. The unsteady angle of attack is provided for comparison. Phase differences between the lift and moment and oscillatory motion can be clearly seen.

B. The NLR 7301 Airfoil

Flow about the NLR 7301 section provides a severe test for the computational method described in preceding sections. Not only is the airfoil exceptionally thick, but the leading edge is extremely blunt. Thus, the assumptions inherent in small disturbance theory may be in violation. Nevertheless, this case was selected because of available existing unsteady experimental data. In order to render the geometry more tractable for a small disturbance calculation, the original airfoil slopes were slightly modified. This modification is discussed in Appendix A and has been used for all the computations presented here with the NLR 7301 airfoil.

Steady state solutions were generated for $M_\infty = 0.75$, $\alpha = 0.37^0$, and $Re_\infty = 1.148 \times 10^7$ in the manner as was described for the RAE 2822 airfoil. These conditions duplicate those of the experiments of Davis and Malcolm[16]. Surface pressure distributions for the respective results and the experimental data appear in Figure 10. Both the inviscid calculations and the wedge solution are seen to agree favorably with experiment upstream of the shock. Location of the shock is poorly predicted by the inviscid result. Without the aforementioned slope modification, the shock was found to lie at the trailing edge. Improvement occurs when the wedge is included. On the lower surface both solutions are seriously deficient. The lag entrainment result appears to predict the shock location reasonably well, but the shock is weaker than that indicated by the experiment. In the aft region, the

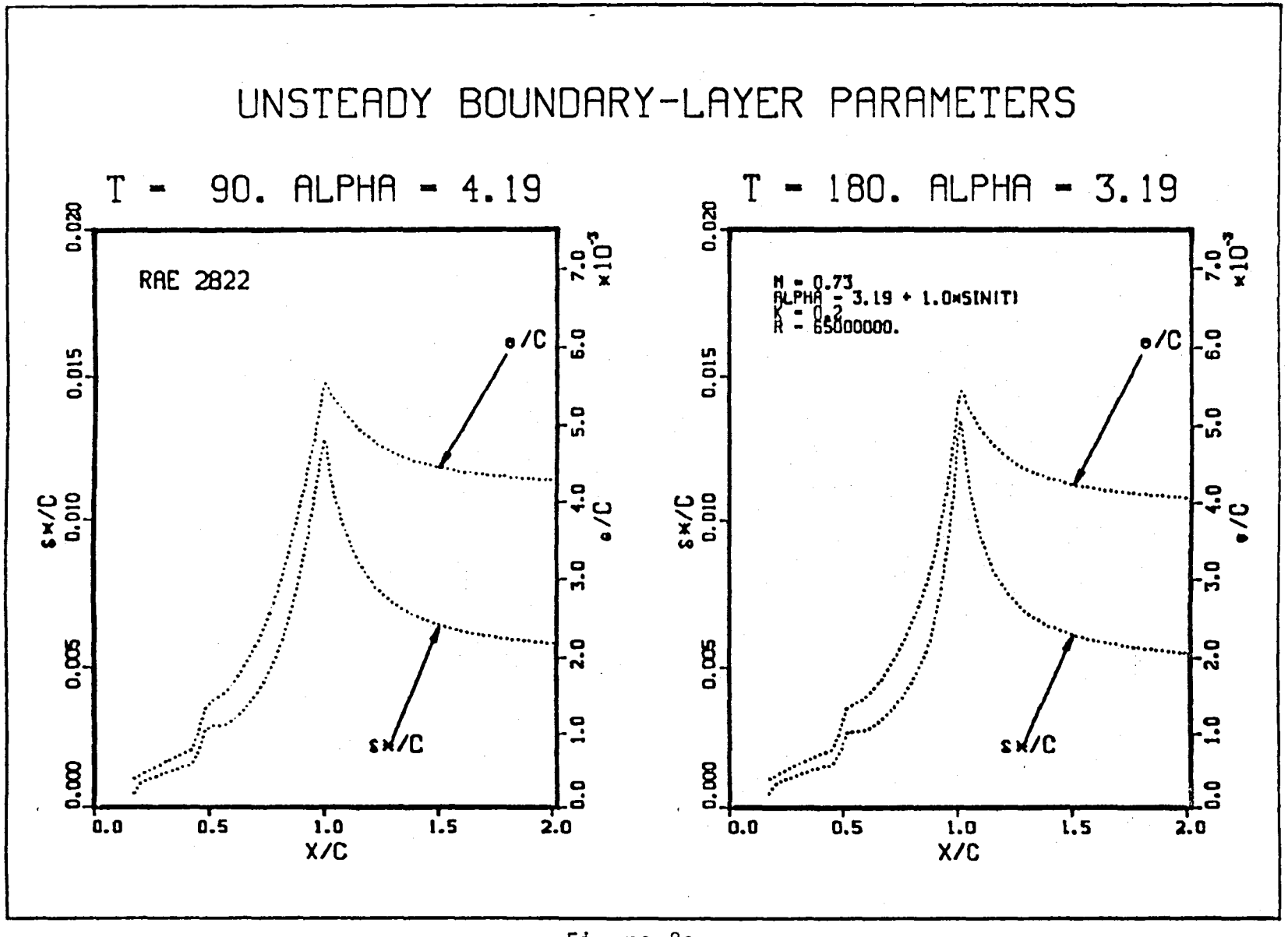
UNSTEADY BOUNDARY-LAYER PARAMETERS
T = 90. ALPHA = 4.19
RAE 2822
θ/C
δ*/C
X/C
T = 180. ALPHA = 3.19
M = 0.73
ALPHA = 3.19 + 1.0*SIN(T)
K = 0.2
R = 65000000.
θ/C
δ*/C
X/C

Figure 8a.

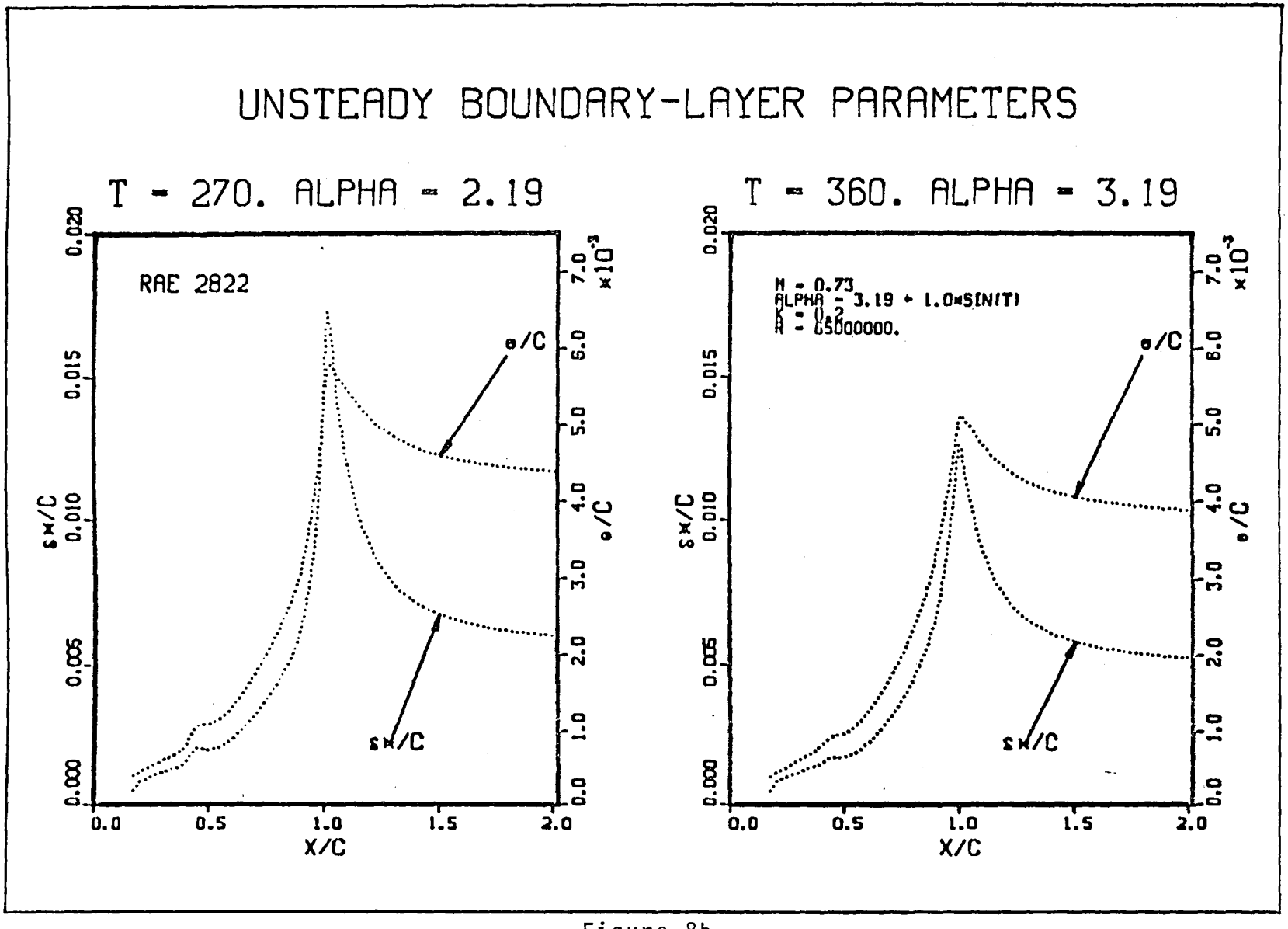
UNSTEADY BOUNDARY-LAYER PARAMETERS
T = 270. ALPHA = 2.19
RAE 2822
θ/C
δ*/C
δ*/C
θ/C
X/C
T = 360. ALPHA = 3.19
M = 0.73
ALPHA = 3.19 + 1.0*SIN(T)
δ*/C
θ/C
X/C

Figure 8b.

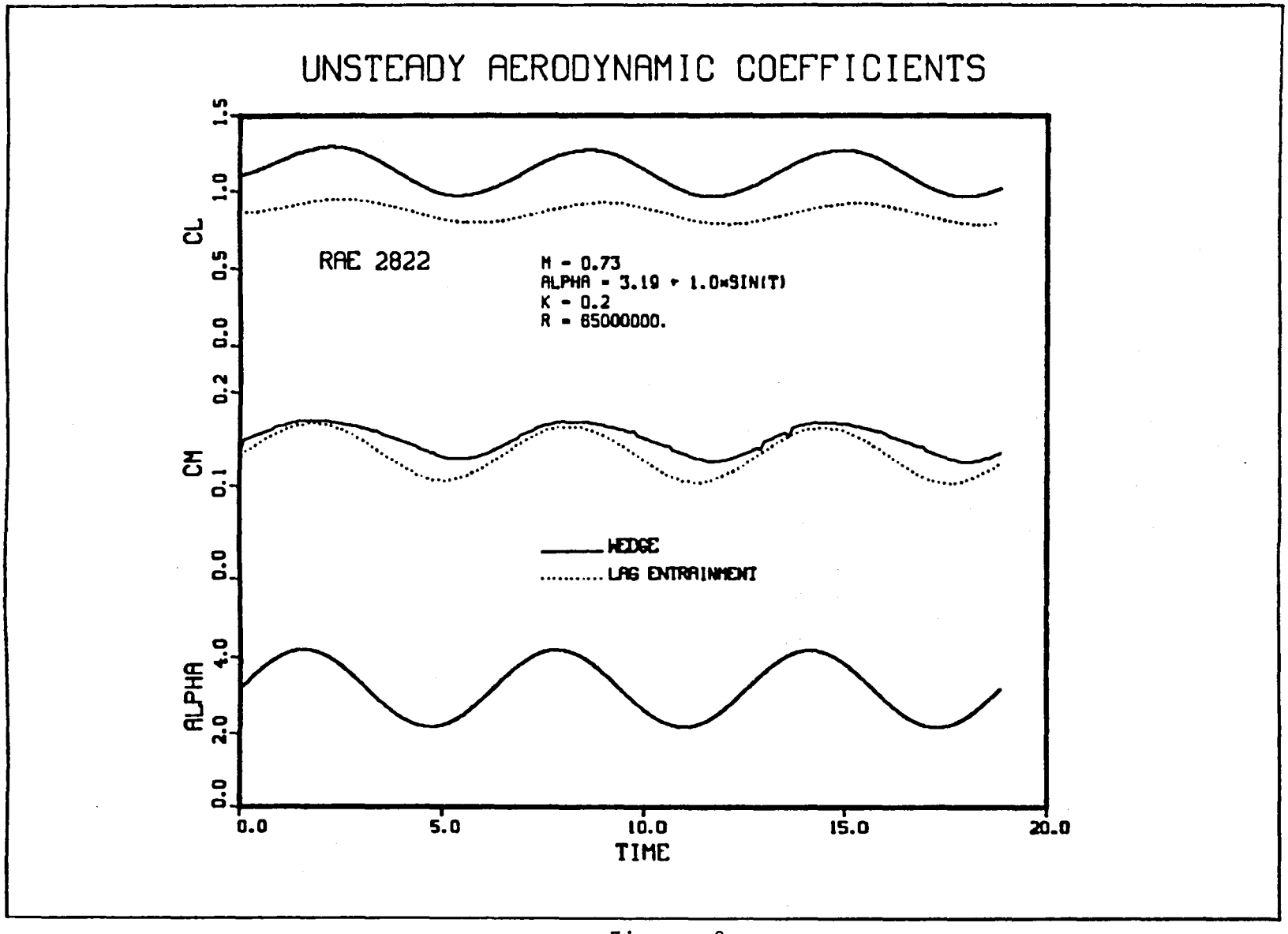
UNSTEADY AERODYNAMIC COEFFICIENTS
CL
CM
ALPHA
1.5
1.0
0.5
0.0
0.2
0.1
0.0
4.0
2.0
0.0
RAE 2822
M = 0.73
ALPHA = 3.19 + 1.0*SIN(T)
K = 0.2
R = 65000000.
WEDGE
LAG ENTRAINMENT
0.0
5.0
10.0
15.0
20.0
TIME

Figure 9.

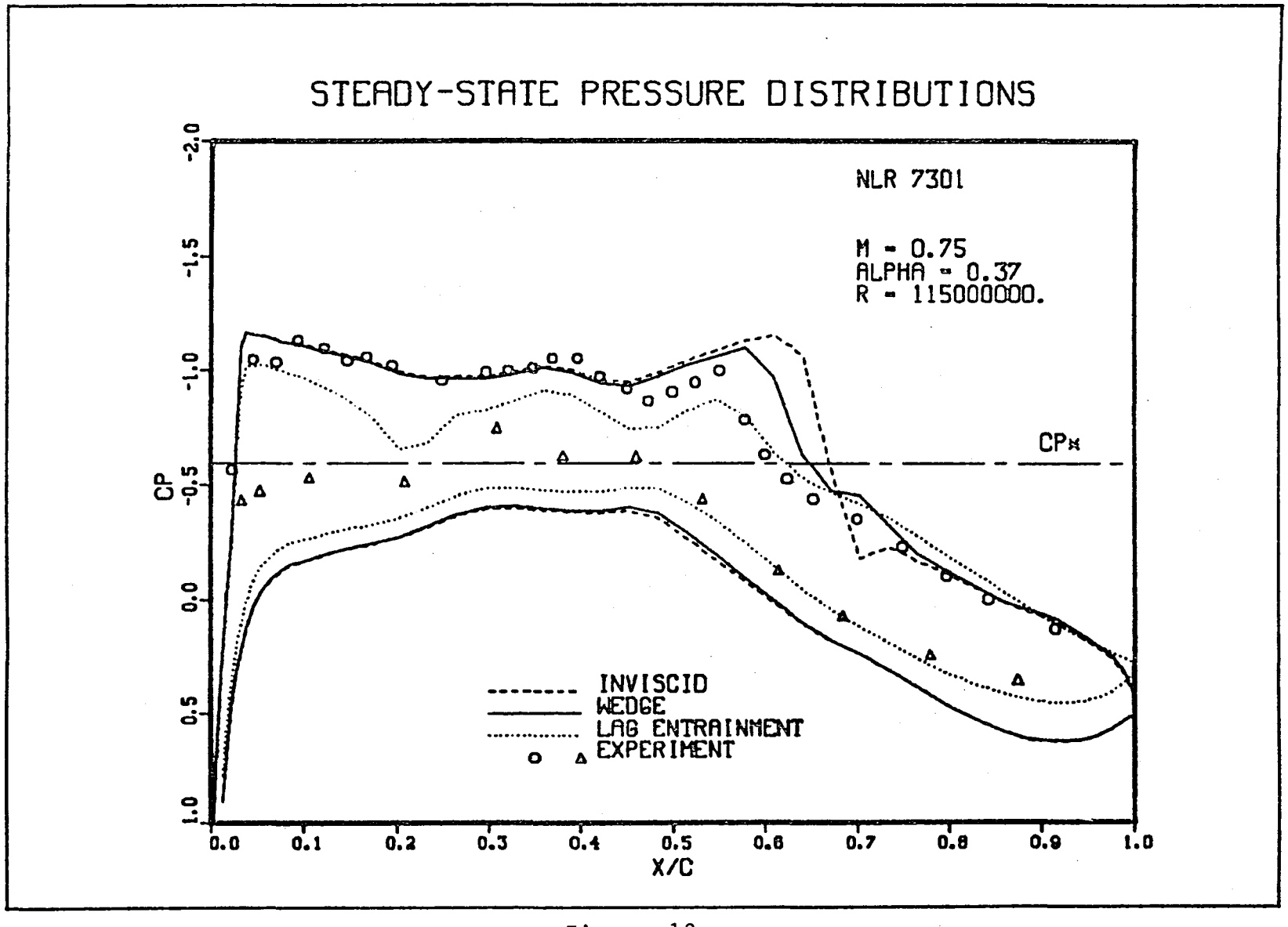
STEADY-STATE PRESSURE DISTRIBUTIONS
NLR 7301
M = 0.75
ALPHA = 0.37
R = 115000000.
CPK
CP
X/C
INVISCID
WEDGE
LAG ENTRAINMENT
EXPERIMENT
-2.0
-1.5
-1.0
-0.5
0.0
0.5
1.0
0.0
0.1
0.2
0.3
0.4
0.5
0.6
0.7
0.8
0.9
1.0

Figure 10.

lag entrainment solution agrees favorably with the data. Upstream, however, there is a discrepancy on both the upper and lower surfaces.

The generally poor agreement between all the computed results and the experimental data is attributed to the limitations of small disturbance theory. This conclusion is supported by a previous result[8] for this same case where it was not possible to match the test data except by performing an inverse calculation. Thus, the good agreement obtained by the inviscid and wedge solutions on the upper surface ahead of the shock must be considered to be fortuitous. It is noted that the lift for these results must necessarily be in serious disagreement with the test. Corresponding viscous parameters for this case from the lag entrainment solution are shown in Figure 11.

Using the steady-state solutions as initial conditions, the airfoil was oscillated sinusoidally in rotation about $x = 0.4$ with a reduced frequency $k = 0.6$ and an amplitude of 0.5^{o}, duplicating one of the unsteady test conditions of Davis and Malcolm. The condition $k = 0.6$ may violate the low frequency approximation, but the range of applicability of the governing equation can easily be extended by including a high frequency term in the surface boundary condition[2]. Three cycles of the pitching oscillation were computed with a value of Δt corresponding to 1^{o} of rotation per time step. Instanteous pressure distributions for the last cycle of oscillation are shown in Figure 12. It is seen that the inviscid and wedge solutions vary only slightly from their respective steady-state values. The lag entrainment distribution, on the other hand, alters considerably during the course of the oscillatory cycle. This is due to the weakened shock which is present and allows for greater pressure fluctuations in the supersonic region. At $t = 270$ it can be seen that the pressure level crosses the sonic value (Cp^*) more than once. Because this criteria is used to define and locate the wedge position of the viscous coupling, special provision had to be made to treat this case. This was done by forcing the code not to consider sonic locations upstream of a fixed value ($x = 0.5$).

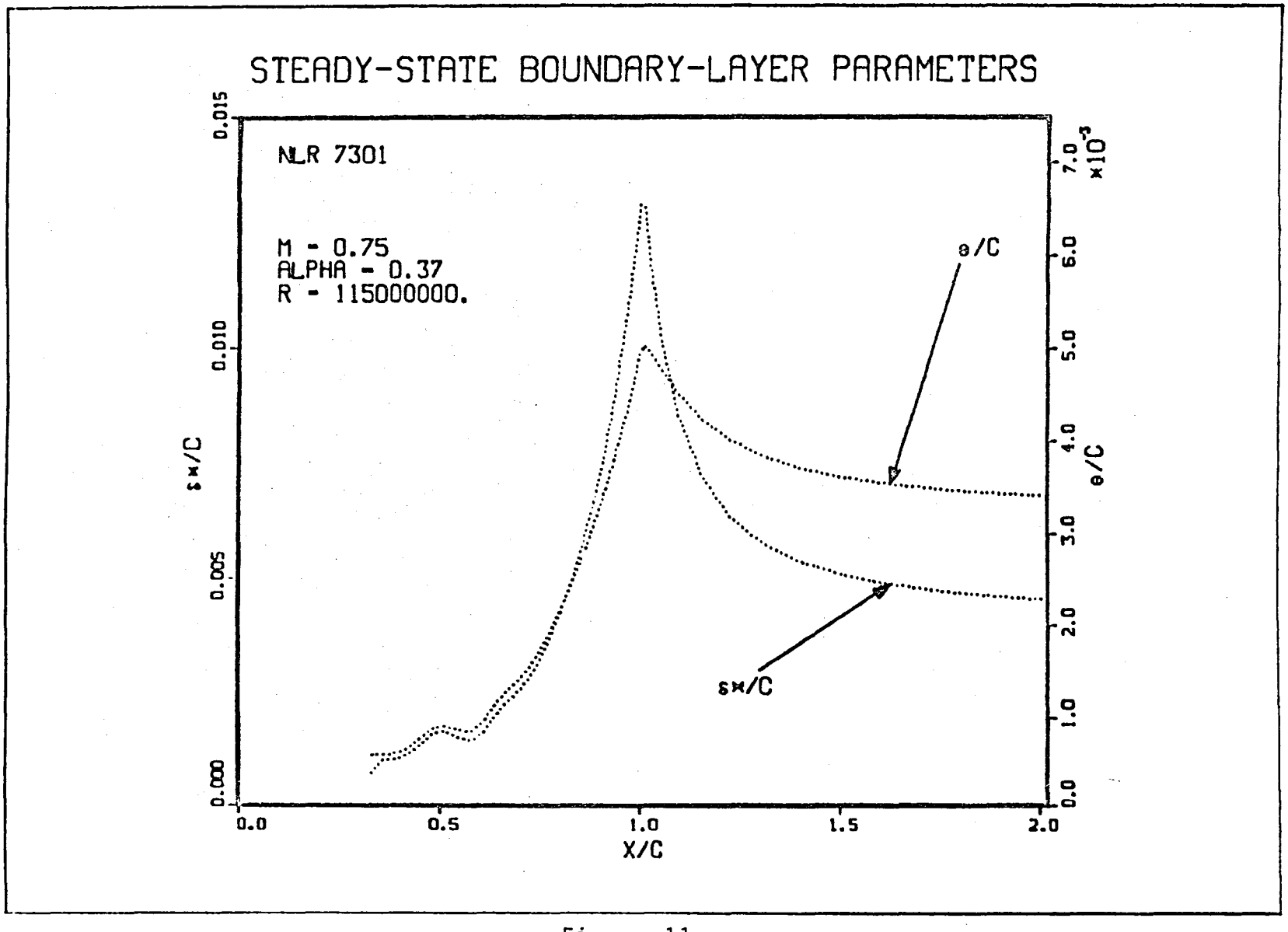
STEADY-STATE BOUNDARY-LAYER PARAMETERS
NLR 7301
M = 0.75
ALPHA = 0.37
R = 115000000.
θ/C
δ*/C
δ*/C
θ/C
X/C
0.000
0.005
0.010
0.015
0.0
1.0
2.0
3.0
4.0
5.0
6.0
7.0
×10⁻³
0.0
0.5
1.0
1.5
2.0

Figure 11.

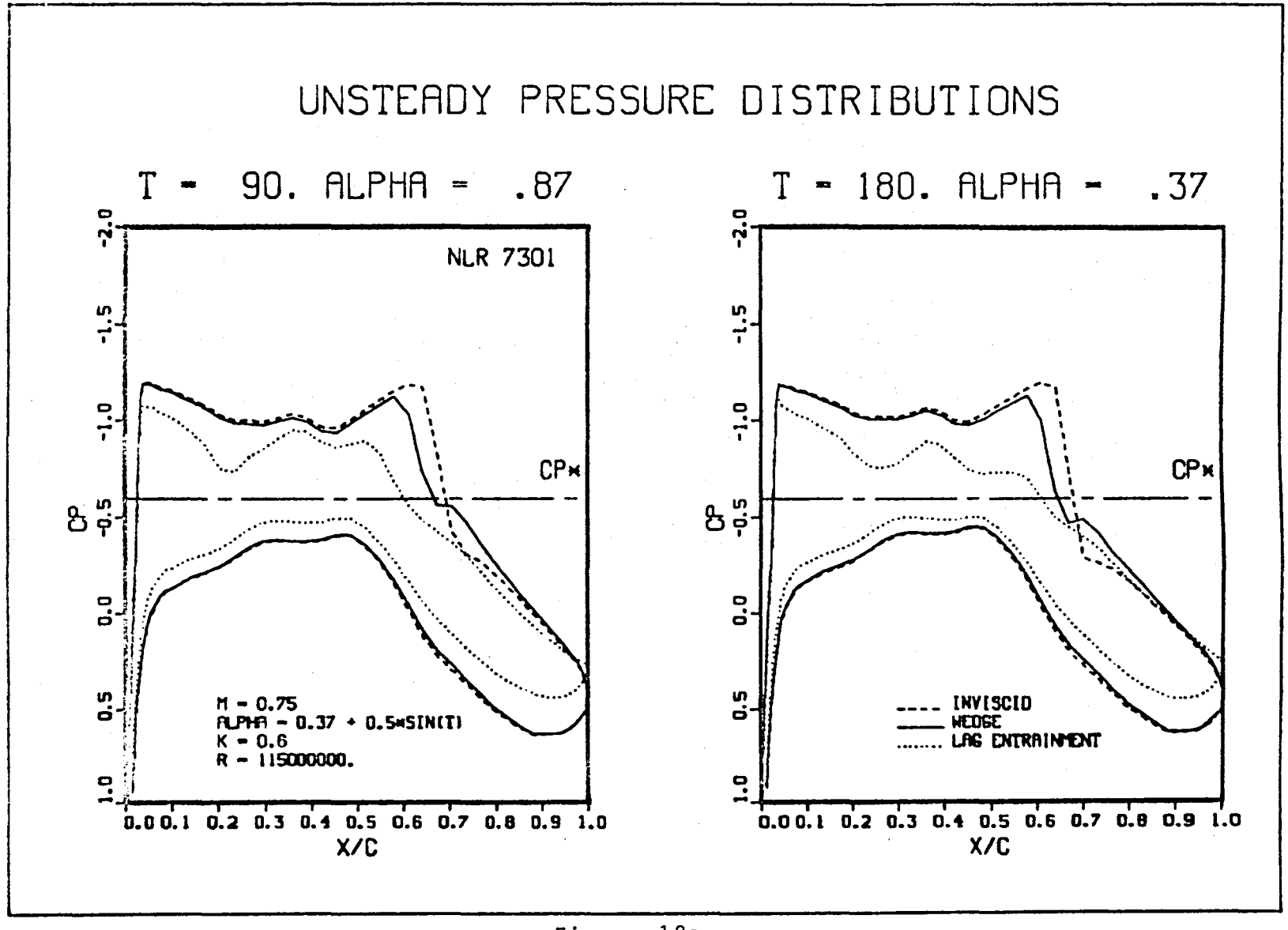
UNSTEADY PRESSURE DISTRIBUTIONS
T = 90. ALPHA = .87
NLR 7301
CP*
M = 0.75
ALPHA = 0.37 + 0.5*SIN(T)
K = 0.6
R = 115000000.
CP
-2.0
-1.5
-1.0
-0.5
0.0
0.5
1.0
0.0 0.1 0.2 0.3 0.4 0.5 0.6 0.7 0.8 0.9 1.0
X/C
T = 180. ALPHA = .37
CP*
INVISCID
WEDGE
LAG ENTRAINMENT
CP
X/C

Figure 12a.

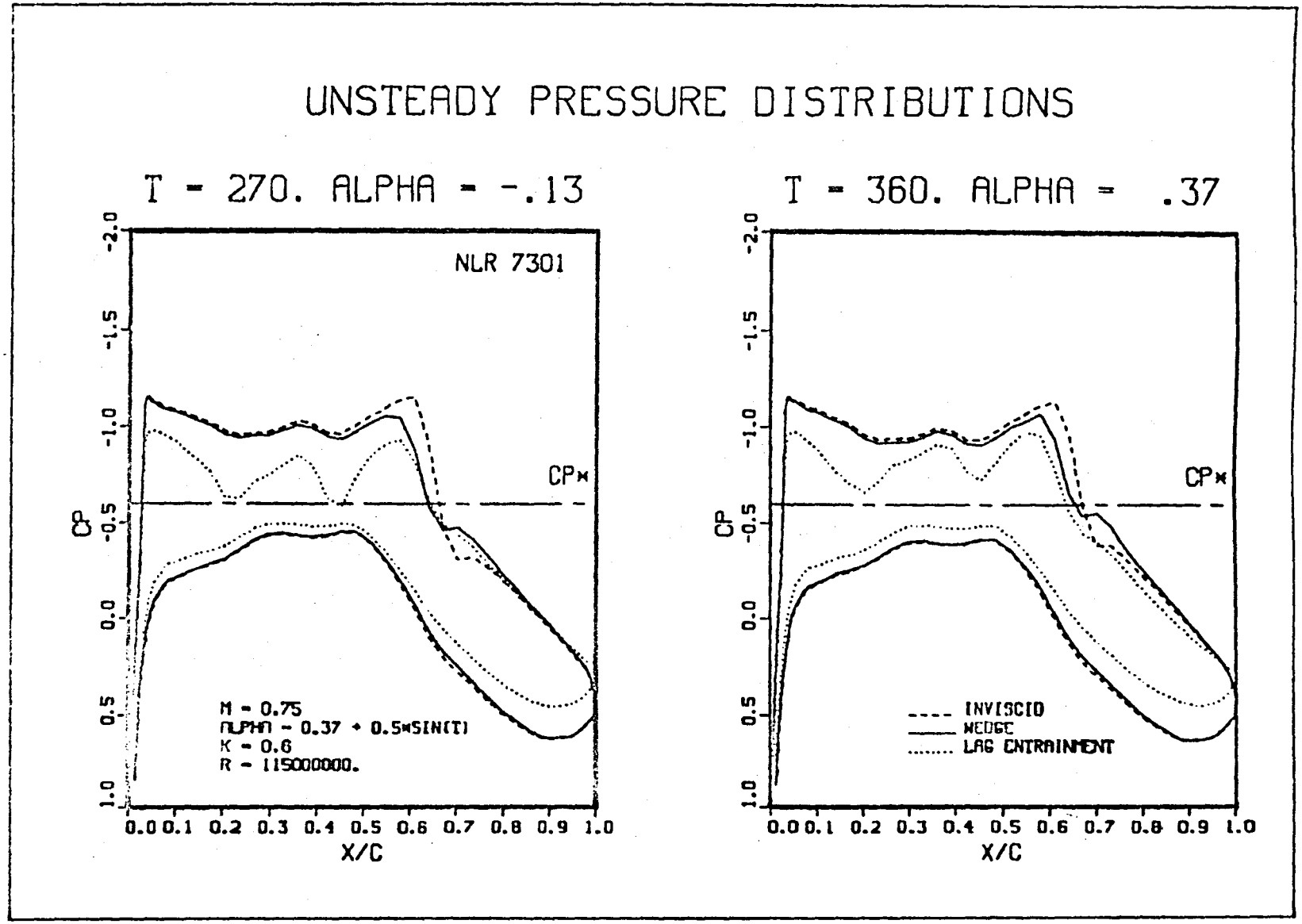
UNSTEADY PRESSURE DISTRIBUTIONS
T = 270. ALPHA = -.13
T = 360. ALPHA = .37
NLR 7301
CP*
CP
-2.0
-1.5
-1.0
-0.5
0.0
0.5
1.0
M = 0.75
ALPHA = 0.37 + 0.5*SIN(T)
K = 0.6
R = 115000000.
INVISCID
WEDGE
LAG ENTRAINMENT
0.0 0.1 0.2 0.3 0.4 0.5 0.6 0.7 0.8 0.9 1.0
X/C

Figure 12b.

A Fourier analysis of all solutions was performed on the upper surface pressure distributions for the last cycle of oscillation and the magnitude and phase of the first Fourier component was extracted. A comparison of these results is shown in Figure 13. In general the lack of agreement with the experiment is considerable. The inviscid solution fails to account for the pressure fluctuations ahead of the shock and also poorly predicts the shock location and pressure level in that region. The wedge solution has some of the same deficiencies, but compares better with the data near the shock and in the aft region. In the case of the lag entrainment result, the previously noted characteristics which were observed in the steady solution result in large fluctuations upstream of and at the shock. It appears that none of the computations have been able to closely reproduce the experimenal data. Once again this is attributed to the limitations of the theory.

Corresponding instantaneous distributions of the boundary-layer parameters appear in Figure 14. Time histories of the instantaneous unsteady lift and moment coefficients and angle of attack are shown in Figure 15. The inviscid and wedge solutions are seen to be quite similar. The lag entrainment solution differs from these not only in magnitude, but also in phase. This is not surprising based on the steady-state results of Figure 10.

A second unsteady oscillating case was calculated for $k = 0.4$ and an amplitude of 1^{o}. Pressure distributions are shown in Figure 16. The results of a Fourier analysis of the upper surface pressure distribution are compared with experiment in Figure 17. It is noted that the characteristics of the magnitude and phase are quite similar to the previous unsteady calculation. The inviscid and wedge solutions do not recover the upstream fluctuations and the inviscid result locates the shock downstream of its experimental value. While the lag entrainment result predicts upstream fluctuations, they are quantitatively inaccurate. In addiition, the phase in aft region does not agree with experiment. Corresponding instantaneous values of θ and δ^* are shown in Figure 18 and time histories of the lift and momentum appear in Figure 19. Phase differences between the respective solutions are apparent.

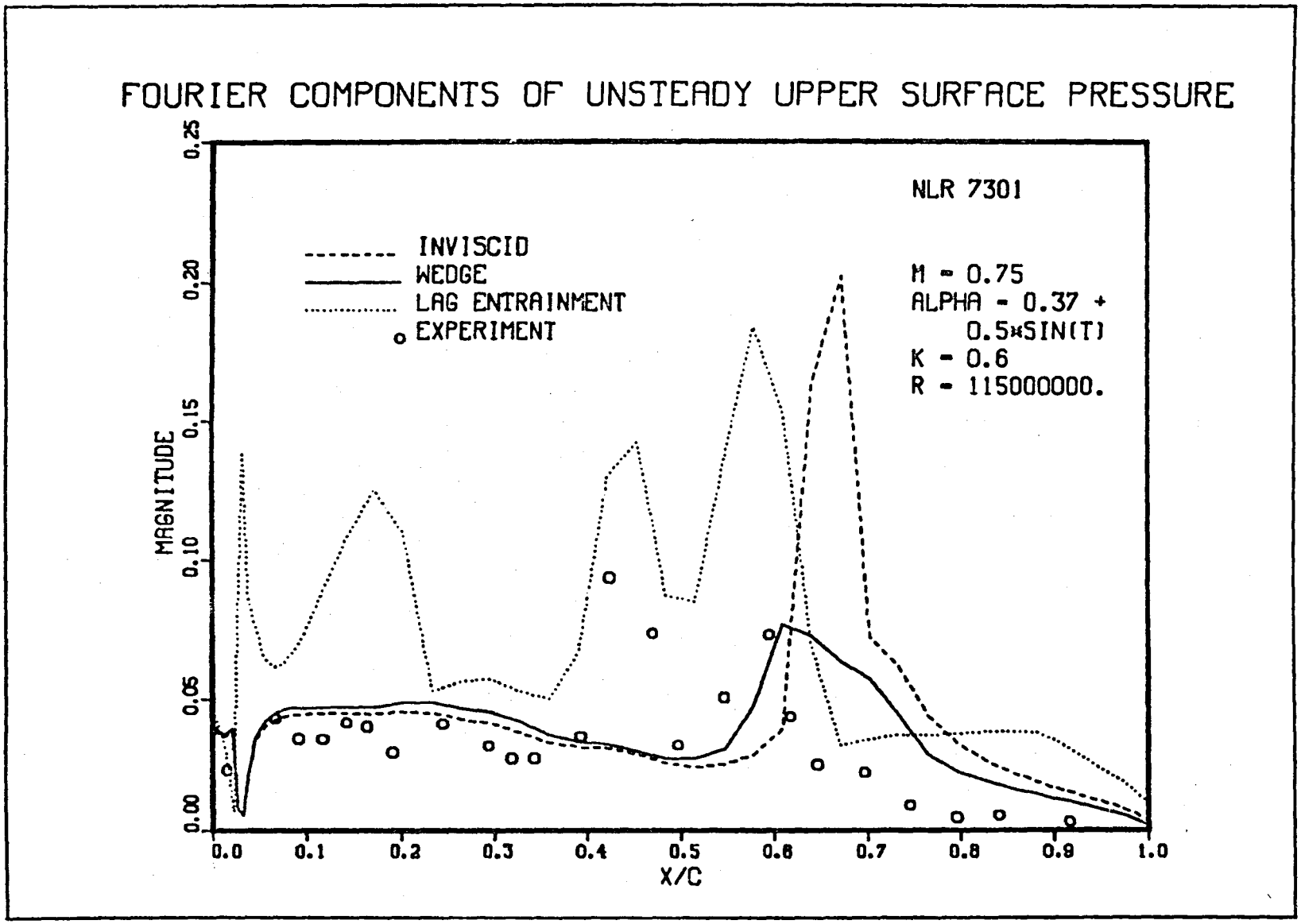
FOURIER COMPONENTS OF UNSTEADY UPPER SURFACE PRESSURE
NLR 7301
INVISCID
WEDGE
LAG ENTRAINMENT
EXPERIMENT
M = 0.75
ALPHA = 0.37 + 0.5*SIN(T)
K = 0.6
R = 115000000.
MAGNITUDE
0.00
0.05
0.10
0.15
0.20
0.25
0.0
0.1
0.2
0.3
0.4
0.5
0.6
0.7
0.8
0.9
1.0
X/C

Figure 13a.

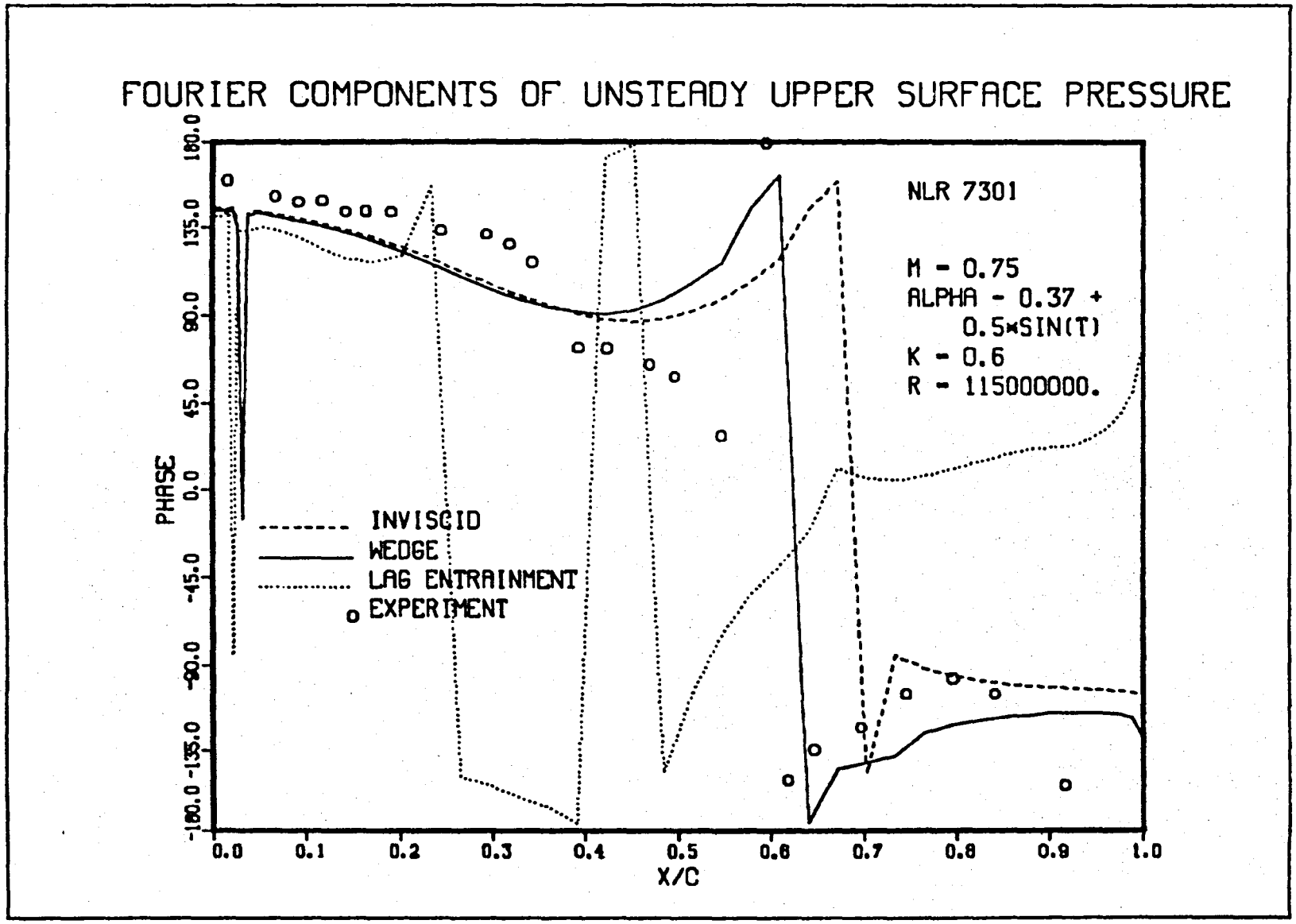
FOURIER COMPONENTS OF UNSTEADY UPPER SURFACE PRESSURE
NLR 7301
M = 0.75
ALPHA = 0.37 + 0.5*SIN(T)
K = 0.6
R = 115000000.
INVISCID
WEDGE
LAG ENTRAINMENT
EXPERIMENT
PHASE
180.0
135.0
90.0
45.0
0.0
-45.0
-90.0
-135.0
-180.0
0.0
0.1
0.2
0.3
0.4
0.5
0.6
0.7
0.8
0.9
1.0
X/C

Figure 13b.

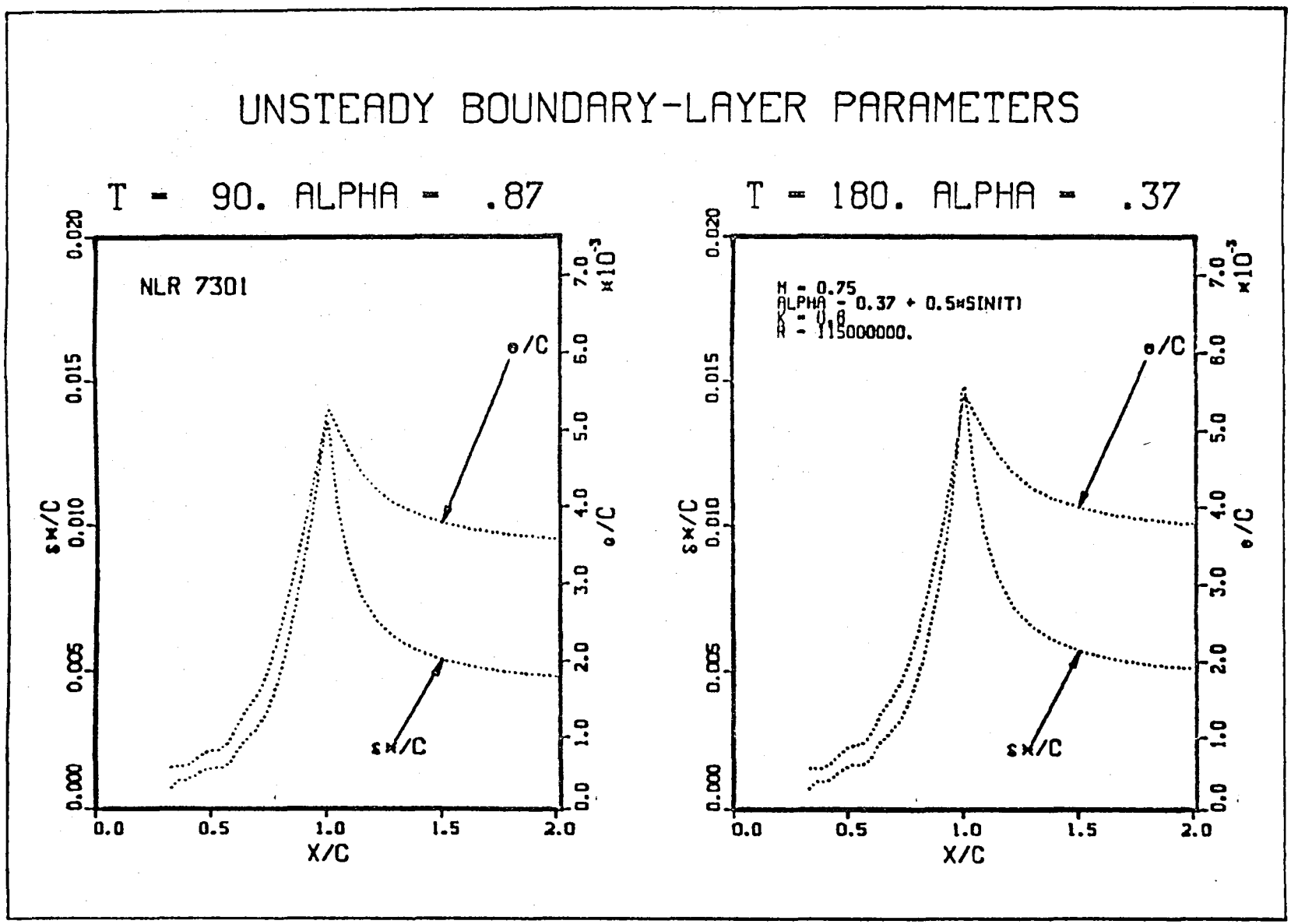
UNSTEADY BOUNDARY-LAYER PARAMETERS
T = 90. ALPHA = .87
NLR 7301
θ/C
δ*/C
δ*/C
θ/C
X/C
T = 180. ALPHA = .37
M = 0.75
ALPHA = 0.37 + 0.5*SIN(T)
K = 0.8
R = 115000000.
θ/C
δ*/C
δ*/C
θ/C
X/C

Figure 14a.

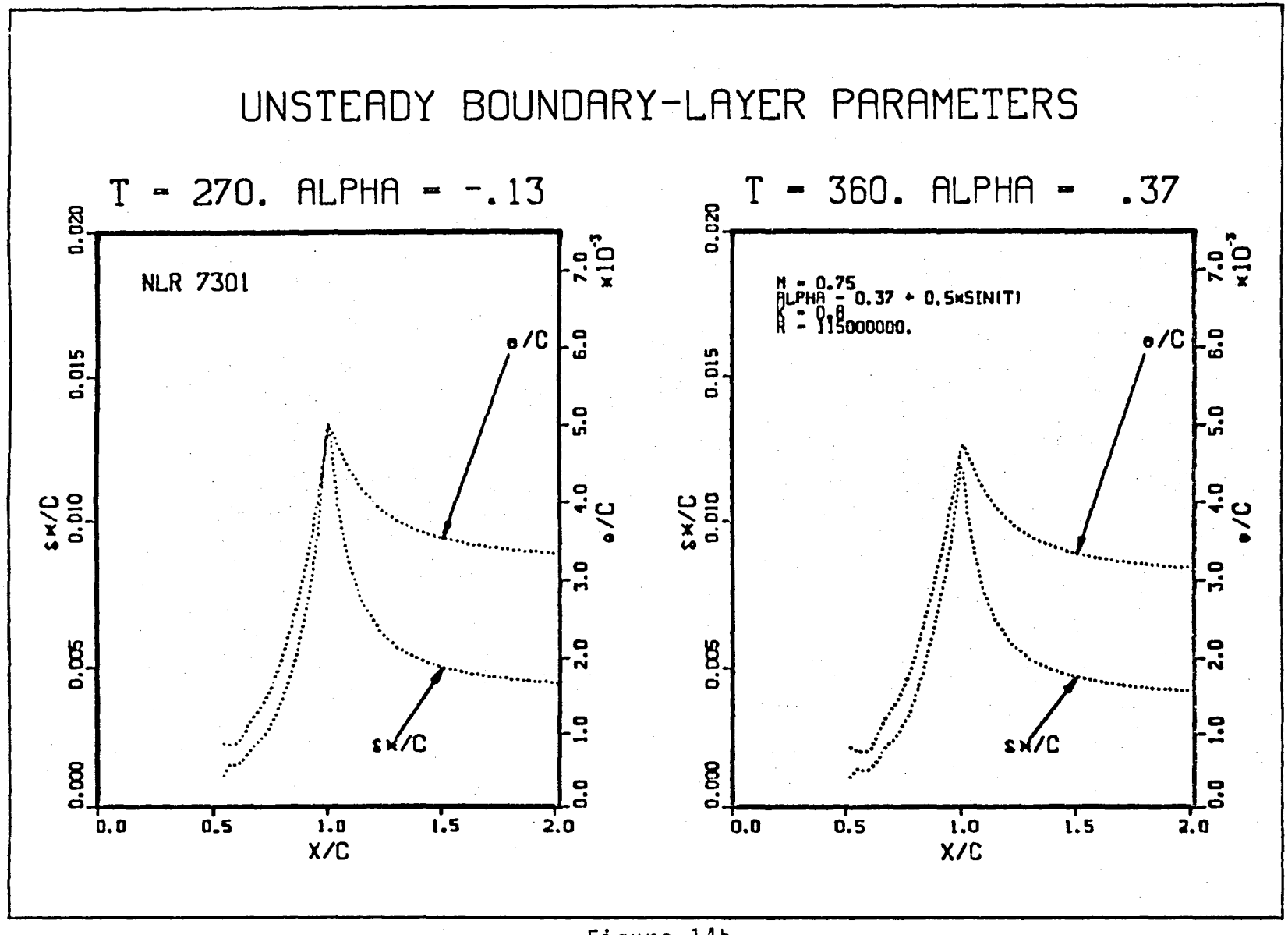
UNSTEADY BOUNDARY-LAYER PARAMETERS
T = 270. ALPHA = -.13
T = 360. ALPHA = .37
NLR 7301
M = 0.75
ALPHA = 0.37 + 0.5*SIN(T)
K = 0.8
R = 15000000.
θ/C
δ*/C
δ*/C
θ/C
X/C
X/C
0.0
0.5
1.0
1.5
2.0
0.000
0.005
0.010
0.015
0.020
0.0
1.0
2.0
3.0
4.0
5.0
6.0
7.0
×10⁻³

Figure 14b.

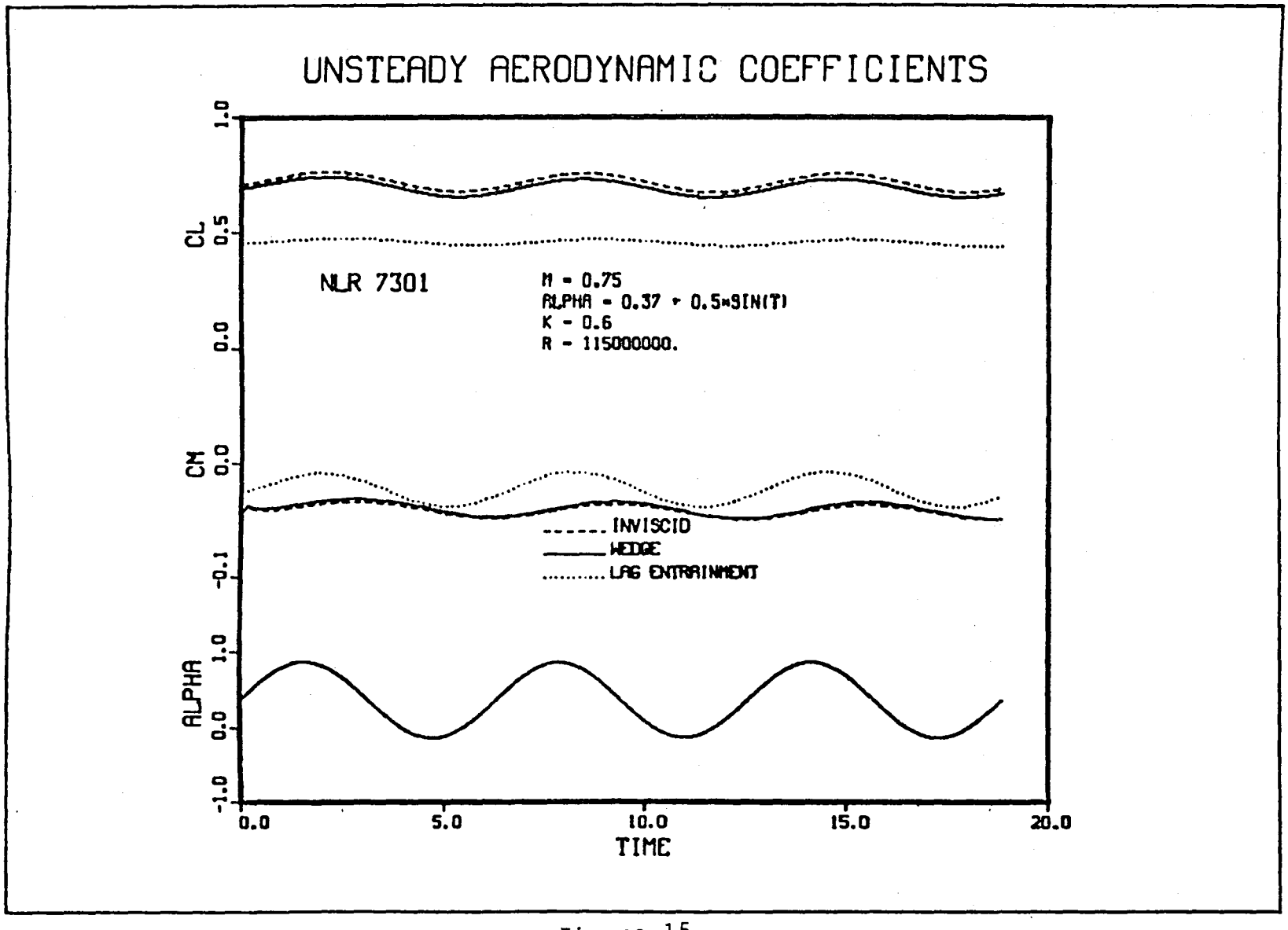
UNSTEADY AERODYNAMIC COEFFICIENTS
CL
CM
ALPHA
1.0
0.5
0.0
-0.1
-1.0
NLR 7301
M = 0.75
ALPHA = 0.37 + 0.5*SIN(T)
K = 0.6
R = 115000000.
INVISCID
WEDGE
LAG ENTRAINMENT
0.0
5.0
10.0
15.0
20.0
TIME

Figure 15.

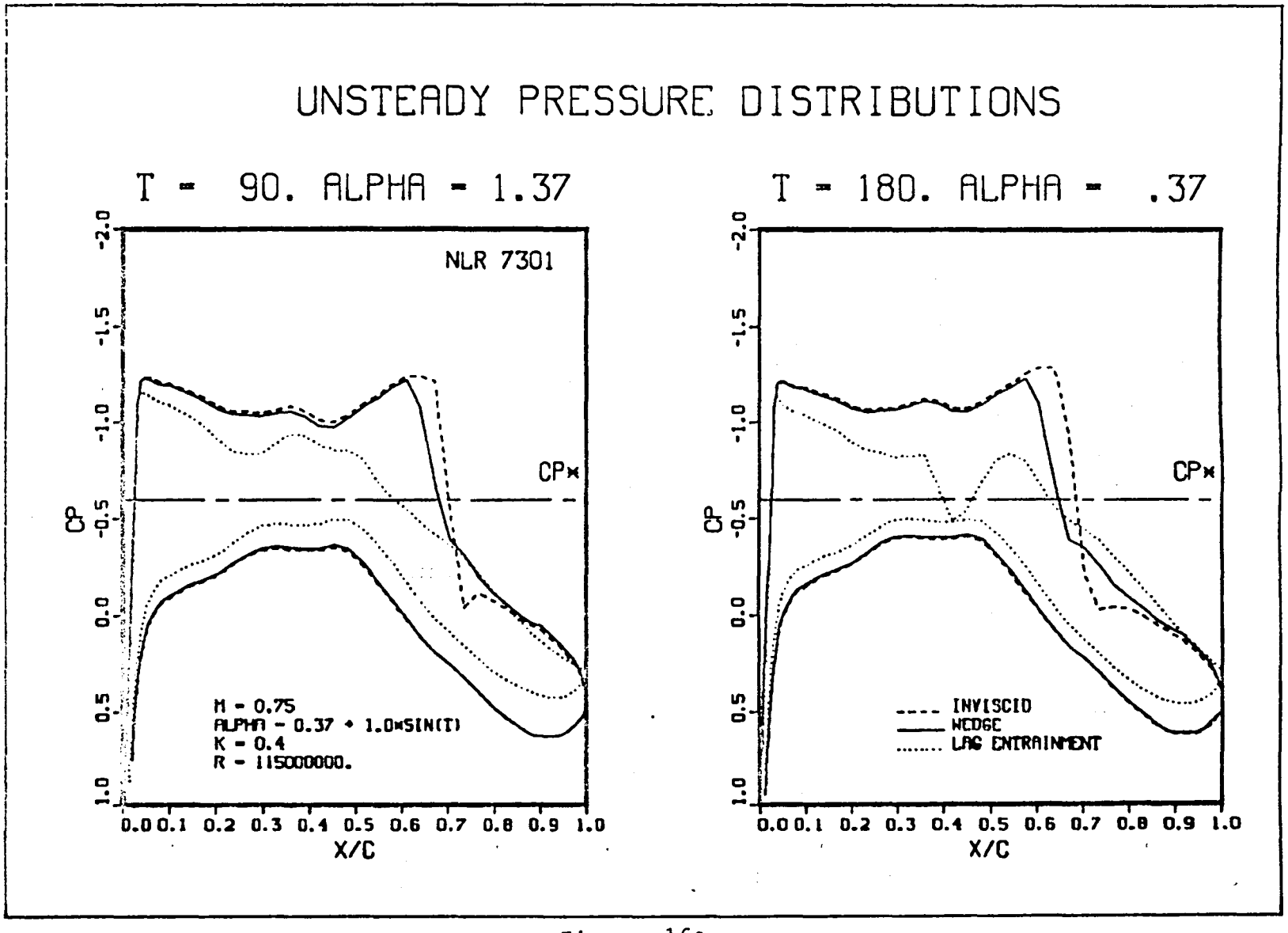
UNSTEADY PRESSURE DISTRIBUTIONS
T = 90. ALPHA = 1.37
NLR 7301
CP*
M = 0.75
ALPHA = 0.37 + 1.0*SIN(T)
K = 0.4
R = 115000000.
CP
X/C
T = 180. ALPHA = .37
CP*
INVISCID
WEDGE
LAG ENTRAINMENT
CP
X/C

Figure 16a.

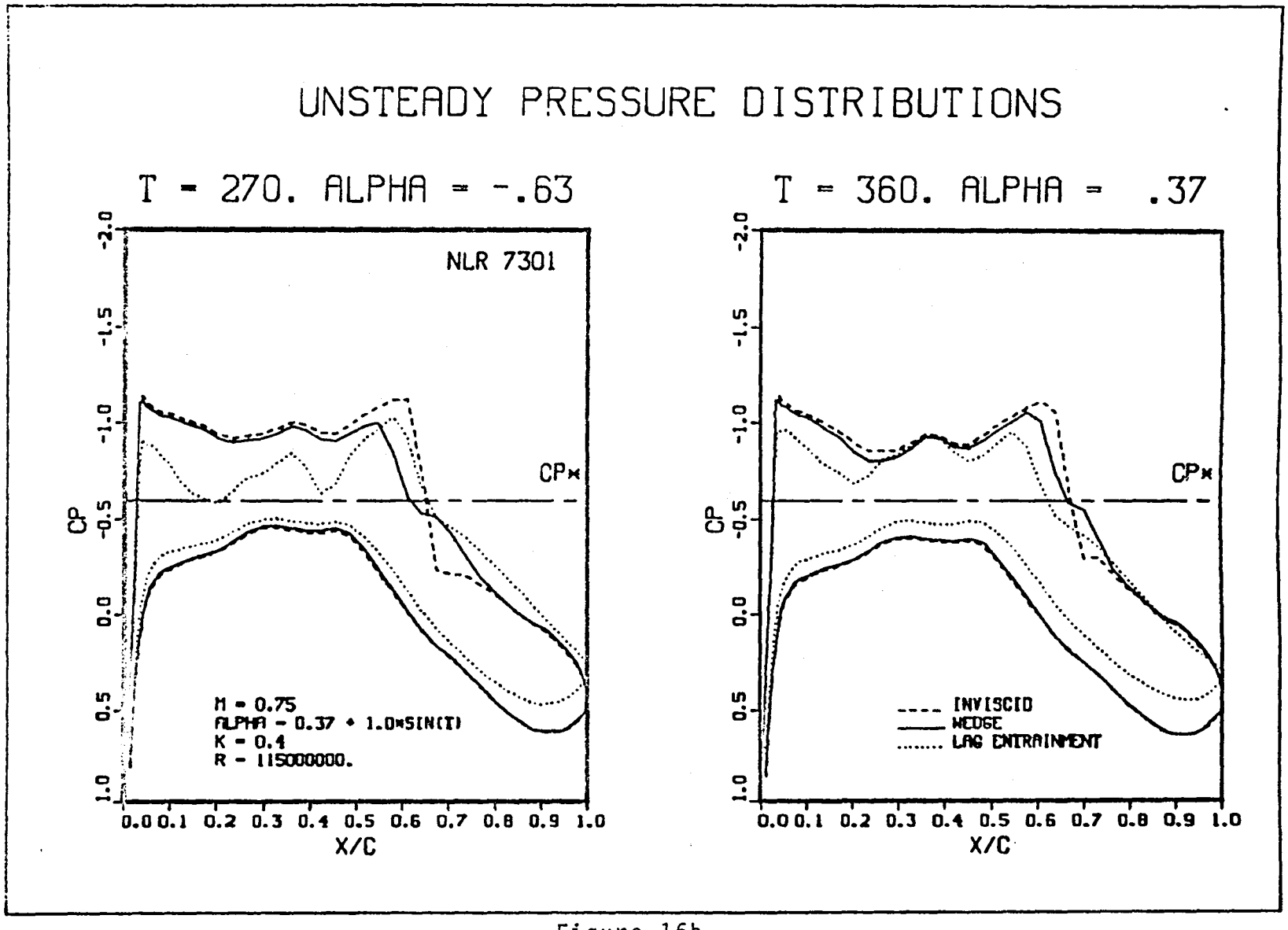
UNSTEADY PRESSURE DISTRIBUTIONS
T = 270. ALPHA = -.63
T = 360. ALPHA = .37
NLR 7301
CP*
CP
X/C
M = 0.75
ALPHA = 0.37 + 1.0*SIN(T)
K = 0.4
R = 115000000.
INVISCID
WEDGE
LAG ENTRAINMENT

Figure 16b.

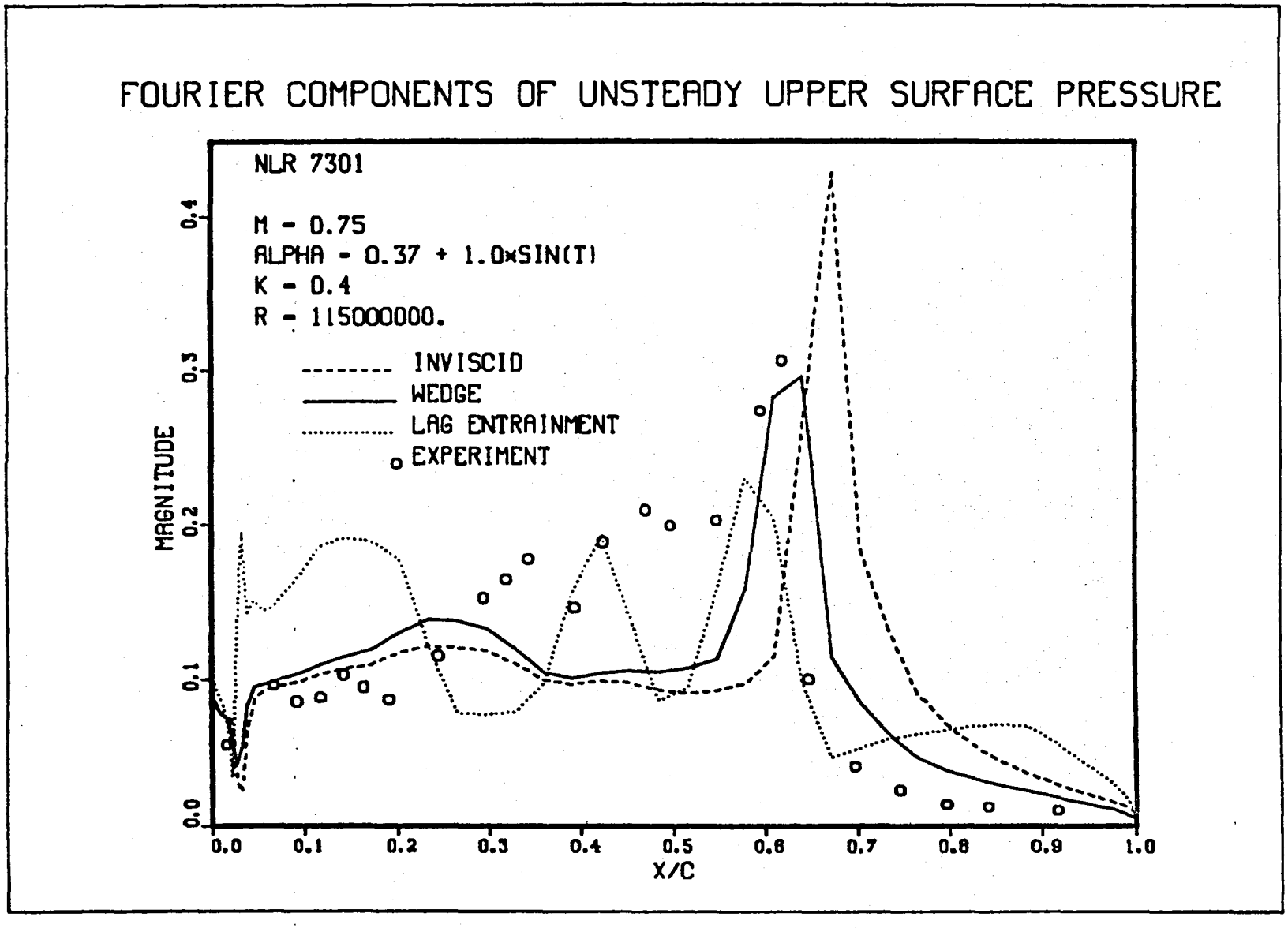
FOURIER COMPONENTS OF UNSTEADY UPPER SURFACE PRESSURE
NLR 7301
M = 0.75
ALPHA = 0.37 + 1.0×SIN(T)
K = 0.4
R = 115000000.
INVISCID
WEDGE
LAG ENTRAINMENT
EXPERIMENT
MAGNITUDE
0.0
0.1
0.2
0.3
0.4
0.5
0.6
0.7
0.8
0.9
1.0
X/C

Figure 17a.

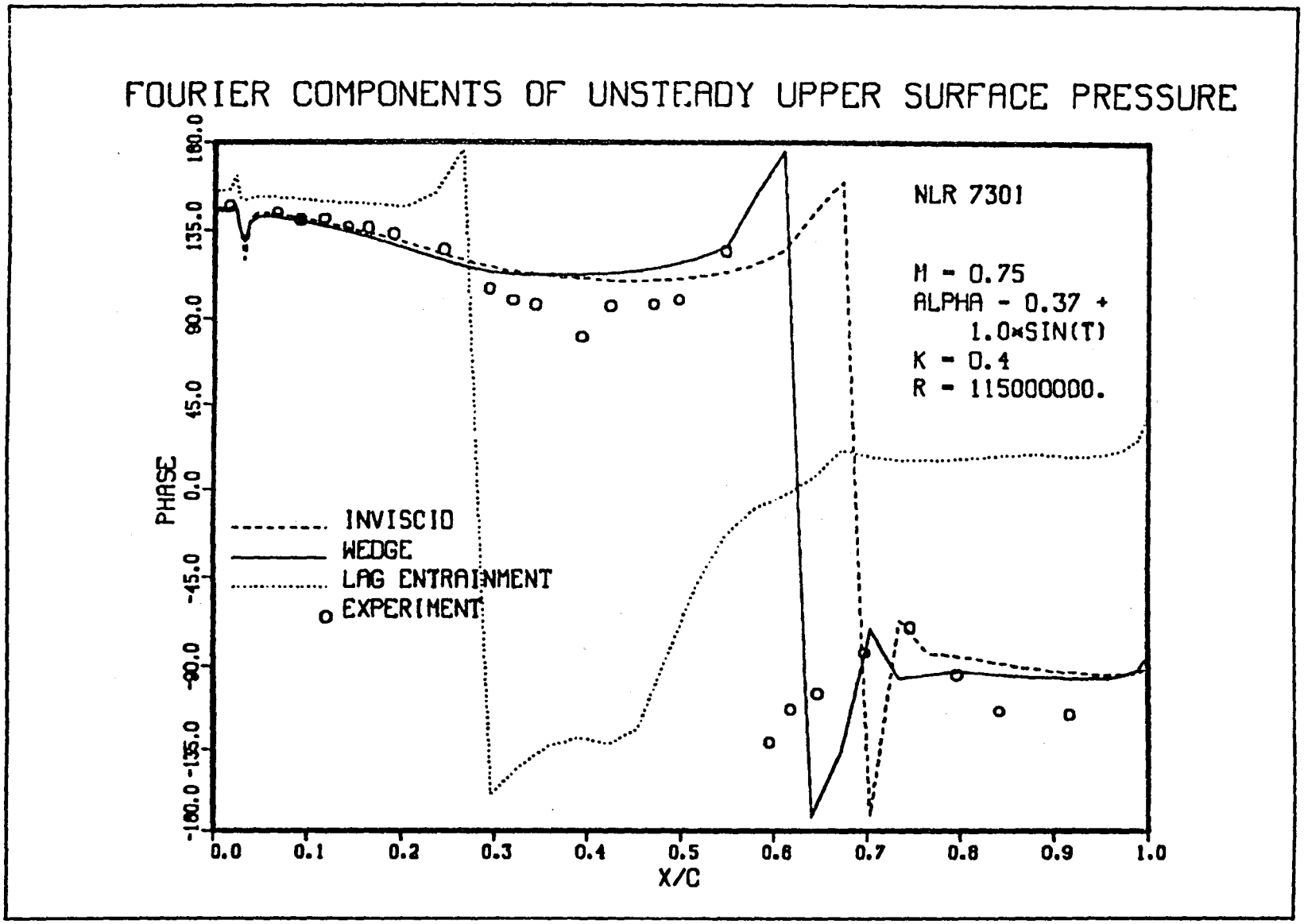
FOURIER COMPONENTS OF UNSTEADY UPPER SURFACE PRESSURE
NLR 7301
M = 0.75
ALPHA = 0.37 + 1.0*SIN(T)
K = 0.4
R = 115000000.
INVISCID
WEDGE
LAG ENTRAINMENT
EXPERIMENT
PHASE
180.0
135.0
90.0
45.0
0.0
-45.0
-90.0
-135.0
-180.0
0.0
0.1
0.2
0.3
0.4
0.5
0.6
0.7
0.8
0.9
1.0
X/C

Figure 17b.

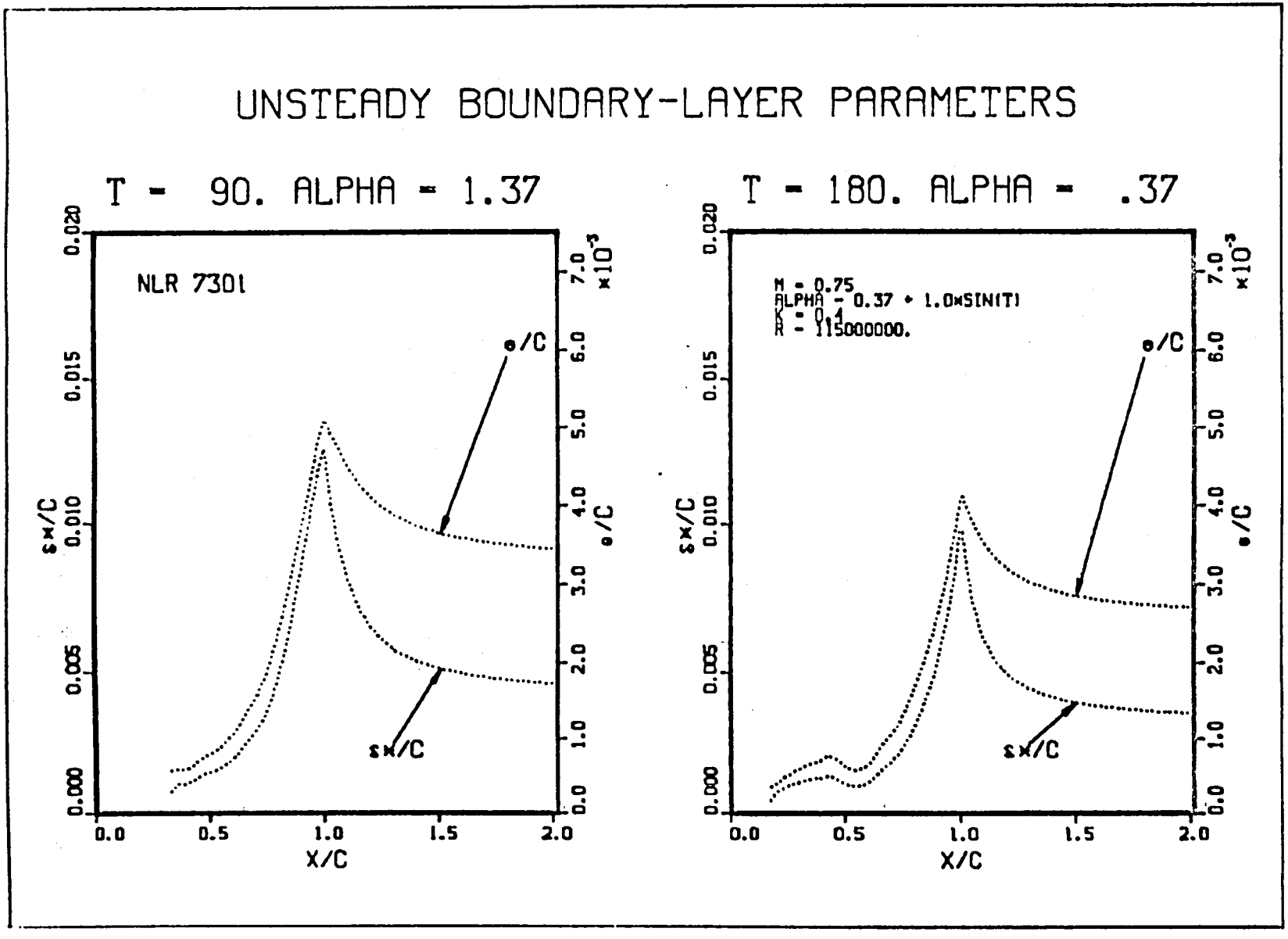
UNSTEADY BOUNDARY-LAYER PARAMETERS
T = 90. ALPHA = 1.37
NLR 7301
θ/C
δ*/C
δ*/C
θ/C
X/C
T = 180. ALPHA = .37
M = 0.75
ALPHA = 0.37 + 1.0*SIN(T)
K = 0.4
R = 115000000.
θ/C
δ*/C
δ*/C
θ/C
X/C

Figure 18a.

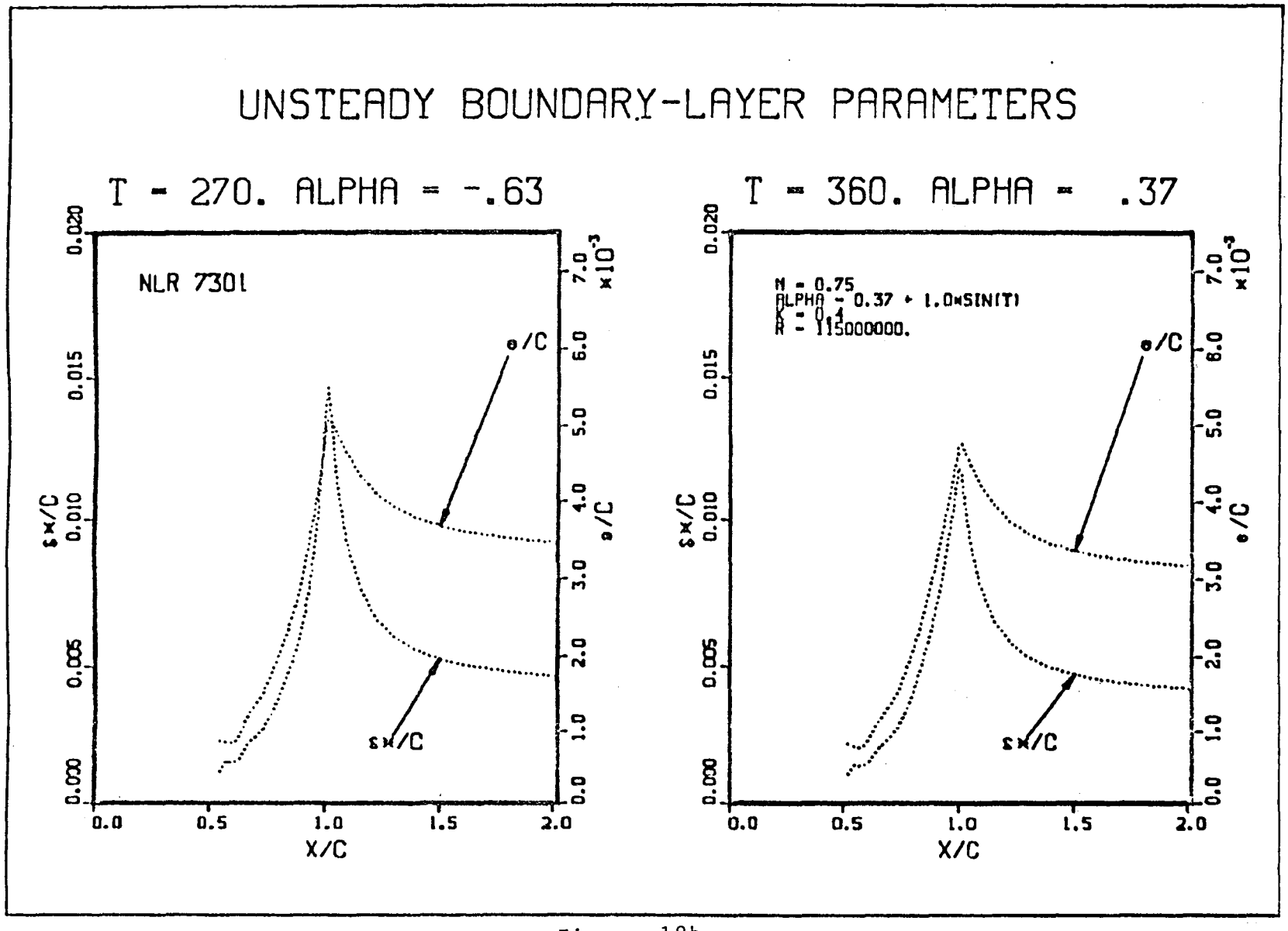
UNSTEADY BOUNDARY-LAYER PARAMETERS
T = 270. ALPHA = -.63
NLR 7301
θ/C
δ*/C
X/C
T = 360. ALPHA = .37
M = 0.75
ALPHA = 0.37 + 1.0*SIN(T)
K = 0.1
R = 115000000.
θ/C
δ*/C
X/C

Figure 18b.

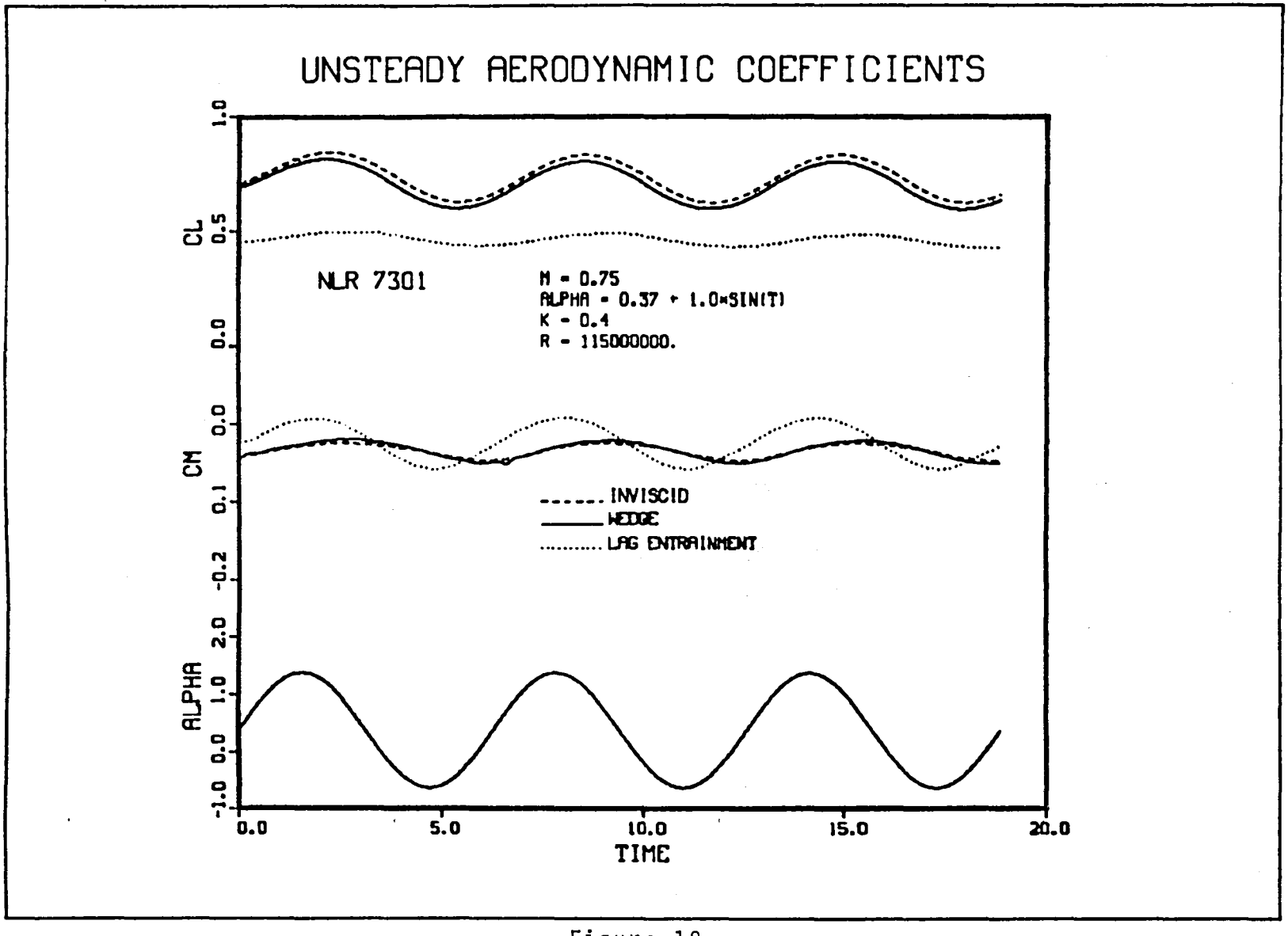
UNSTEADY AERODYNAMIC COEFFICIENTS
CL
CM
ALPHA
1.0
0.5
0.0
0.0
0.1
-0.2
2.0
1.0
0.0
-1.0
NLR 7301
M = 0.75
ALPHA = 0.37 + 1.0*SIN(T)
K = 0.4
R = 115000000.
INVISCID
WEDGE
LAG ENTRAINMENT
0.0
5.0
10.0
15.0
20.0
TIME

Figure 19.

V. CONCLUSIONS AND DISCUSSIONS

Two methods have been considered for including viscous effects in the compuation of unsteady transonic flows. One employs a simple phenomenological model as a computational artifice in accounting for the gross dominant effects of shock-boundary-layer interaction. The second, used in conjunction with the first, utilizes an additional set of integral equations to treat displacement effects of aft cambered regions and viscous trailing wakes witin the context of boundary-layer theory. Theoretical developments of the methods have been presented and modifications for their inclusion in the LTRAN2 code have been described. While the methods considered are relatively simple they are thought to model the significant effects of viscosity and thus be useful for aeroelastic applications without degrading numerical efficiency.

A number of computational results for both steady and unsteady flows have been generated. Comparisons with inviscid solutions and experimenal data have been made. Results which duplicate previous steady cases compare favorably, thus ensuring the integrity of modifications to the code. The unsteady calculations for the NLR 7301 airfoil exhibited serious deficiencies compared to experimental data. Although this result was not surprising, it is attributed to the severity of the case which may have violated some of the inherent theoretical assumptions. It is suggested that other unsteady computations be performed for a more thorough understanding of the limitations of the methods.

All of the calculations presented here were carried out on the NASA AMES Research Center CDC 7600 computing system. Solutions for the wedge model were generated in virtually the same computational times as those for the inviscid LTRAN2 code. Inclusion of the lag entrainment equations required approximately 10% additional computing time. Thus, the goal of maintaining efficiency appears to have been met. It is hoped that the modified code can thus extend the utility of LTRAN2 for the computation of unsteady transonic flows when viscous effects of shock-boundary-layer interaction, aft displacement, and trailing wakes are not negligible.

REFERENCES

1. Ballhaus, W. F. and Goorjian, P. M., "Implicit Finite-Different Computations of Unsteady Transonic Flows about Airfoils," AIAA Journal, Vol. 15, Dec. 1977, pp 1728-1735.

2. Rizzetta, D. P. and Yoshihara, H., "Computations of the Pitching Oscillation of a NACA 64A010 Airfoil in the Small Disturbance Limit," AIAA Paper 80-0128, Pasadena, California, Jan. 1980.

3. Mason, W. H., Ballhaus, W. F., MacKenzie, C., Frick, J., and Stern, M., "An Automated Procedure for Computing the Three-Dimensional Transonic Flow Over Wing-Body Combinations, Including Viscous Effects," AFFDL-TR-122, Vol. I, Feb, 1977.

4. Green, J. E., Weeks, D. J., and Brooman, J. W. F., "Prediction of Turbulent Boundary Layers and Wakes in Compressible Flow by a Lag-Entrainment Method," RAE Reports and Memoranda No. 3791, Jan. 1973.

5. East, L. F., Smith, P. D., and Merryman, P. J., "Prediction of the Development of Separated Turbulent Boundary Layers by the Lag-Entrainment Method," RAE Technical Report 77046, Mar. 1977.

6. Wai, J. C. and Yoshihara, H., "Viscous Transonic Flow over Airfoils," Proceedings of the Seventh International Conference on Numerical Methods in Fluid Dynamics, Palo Alto, California, June 1980.

7. Wai, J. C., and Yoshihara, H., "Planar Transonic Airfoil Computations with Viscous Interactions," AGARD Conference Proceedings, Computation of Viscous-Inviscid Interactions, Colorado Springs, Colorado, Sept. 1980.

8. Rizzetta, D. P. and Yoshihara, H., "Oscillating Supercritical Airfoils in the Transonic Regime with Viscous Interactions," AGARD Conference Proceedings, Boundary Layer Effects on Unsteady Airloads, Aix-en-Provence, France, Sept. 1980.

9. Green, J. E., "Application of Head's Entrainment Method to the Prediction of Turbulent Boundary Layers and Wakes in Compressible Flow," RAE Reports and Memoranda No. 3788, Apr. 1972.

10. Bradshaw, P., Ferriss, D. H., and Atwell, N. P., "Calculation of Turbulent Boundary-Layer Development Using the Turbulent Energy Equation," Journal of Fluid Mechanics, Vol. 28., 1967, pp 593-616.

11. Head, M. R., "Entrainment in the Turbulent Boundary Layer," ARC Reports and Memoranda No. 3152, 1958.

12. Collyer, M. and Lock, R., "Prediction of Viscous Effects in Steady Transonic Flows Past an Airfoil," Aeronautical Quarterly, Vol. 30, Part 3, 1979.

13. "Equations, Tables, and Charts for Compressible Flow," NACA Report 1135, 1953.

14. Schlichting, H., Boundary Layer Theory, McGraw-Hill Book Company Inc., New York, 1960, pp 536-537.

15. Cook, P. H., McDonald, M. A., and Firmin, M. C. P., "Aerofoil RAE 2822-Pressure Distributions and Boundary Layer and Wake Mesurements," AGARD-AR-138.

16. Davis, S. S. and Malcolm, G. N., "Experimental Unsteady Aerodynamics of Conventional and Supercritical Airfoils," NASA Technical Memorandum 81221, Aug. 1980.

17. LeBalleur, J. C., "Calcul des Ecoulements a Fortes Interaction Visqueuse au Moyen de Methodes de Couplage," AGARD-CP-291, Oct. 1980.

18. Riegels, F., "Das Umstromungsproblem bei inkompressiblen Potentialstromungen," Ing. - Archiv., Bd. XVI, 1948, pp 373-376.

APPENDIX A

At the leading edge of all blunt-nosed airfoils, the surface slope becomes infinite. Because this slope provides the flow tangency condition, the basic assumptions of small disturbance theory are violated in this region. Thus, since the solution in the immediate neighborhood of the leading edge cannot be described correctly by a numerical integration of the governing equation, a modification of the surface slope near the nose is often employed in transonic calculations. Such modifications are applied locally to enhance stability without degrading the results outside of the leading edge region.

One of the most common of these modifiations is the Riegels' rule[18]. If $f^{\pm}_{xo}$ is the original airfoil surface slope, then the modified slope $f^{\pm}_{xm}$ is computed according to the following formula:

$$f_{xm}^{\pm} = f_{xo}^{\pm} \left[1 + (f_{xo}^{\pm})^2\right]^{-1/2} .$$

This expression alters the slope in a smooth continuous manner at all points along the airfoil surface. When the slope is very large (i.e., near the leading edge) it is reduced to unity in the limit of $f^{\pm}_{xo} \to \infty$. Elsewhere, when the slope is small, little change occurs. In the limit $f^{\pm}_{x_o} \to 0$, $f^{\pm}_{xm} = f^{\pm}_{xo}$. Although the basis for Riegels' rule is incompressible theory, it has been widely used for computing steady transonic flows. For completeness, the modified and unmodified surface slopes for the NLR 7301 airfoil which were used for all the computations presented are given below. The unmodified slopes are those generated at computational mesh points by the LTRAN2 code which employs a cubic spline fit through airfoil coodinates for this purpose.

x	f^{+}_{xo}	f^{+}_{xm}	f^{-}_{xo}	f^{-}_{xm}
0.00250	3.11794	0.95222	-3.05200	-0.95029
0.00750	1.78953	0.87295	-1.42208	-0.81800
0.01250	1.33984	0.80140	-0.90111	-0.66942
0.01750	0.96358	0.69387	-0.66624	-0.55445
0.02250	0.75954	0.60485	-0.61575	-0.52432
0.02750	0.67158	0.55752	-0.51744	-0.45956
0.03250	0.52192	0.46269	-0.46085	-0.41854
0.03813	0.38352	0.35809	-0.41565	-0.38381
0.04563	0.34466	0.32585	-0.35792	-0.33699
0.05500	0.27566	0.26575	-0.29837	-0.28591
0.06500	0.23412	0.22796	-0.26036	-0.25196
0.07500	0.20572	0.20150	-0.23001	-0.22416
0.08563	0.18233	0.17937	-0.20005	-0.19617
0.09875	0.15831	0.15637	-0.17457	-0.17197
0.11703	0.13440	0.13321	-0.15341	-0.15164
0.14204	0.11412	0.11339	-0.12556	-0.12458
0.17188	0.09122	0.09084	-0.10286	-0.10232
0.20313	0.07817	0.07793	-0.08716	-0.08683
0.23438	0.07083	0.07065	-0.07088	-0.07070
0.26563	0.05150	0.05143	-0.05092	-0.05085
0.29688	0.03627	0.03624	-0.02748	-0.02747
0.32813	0.02288	0.02287	-0.00449	-0.00449
0.35938	0.00028	0.00028	0.01371	0.01370
0.39063	-0.01312	-0.01312	0.02928	0.02927
0.42188	-0.01191	-0.01191	0.04426	0.04422
0.45313	-0.01294	-0.01294	0.06119	0.06108
0.48438	-0.02988	-0.02987	0.09409	0.09368
0.51563	-0.05300	-0.05293	0.12610	0.12511
0.54688	-0.07613	-0.07591	0.15442	0.15262
0.57813	-0.09763	-0.09717	0.18383	0.18080
0.60938	-0.12661	-0.12561	0.20768	0.20334
0.64063	-0.14333	-0.14188	0.22189	0.21662

x	f^{+}_{xo}	f^{+}_{xm}	f^{-}_{xo}	f^{-}_{xm}
0.67188	-0.15362	-0.15184	0.21845	0.21342
0.70313	-0.16744	-0.16514	0.21495	0.21015
0.73438	-0.19029	-0.18694	0.21649	0.21159
0.76563	-0.20953	-0.20508	0.20620	0.20195
0.79688	-0.21820	-0.21319	0.18921	0.18591
0.82813	-0.23116	-0.22522	0.15643	0.15455
0.85797	-0.23315	-0.22706	0.12979	0.12871
0.88235	-0.23304	-0.22696	0.09068	0.09031
0.90000	-0.23274	-0.22668	0.06194	0.06182
0.91500	-0.23253	-0.22649	0.04077	0.04074
0.93000	-0.23214	-0.22613	0.01876	0.01876
0.94500	-0.22968	-0.22385	-0.00639	-0.00639
0.96000	-0.22468	-0.21921	-0.03459	-0.03457
0.97500	-0.22097	-0.21576	-0.05940	-0.05930
0.98875	-0.22569	-0.22015	-0.07582	-0.07560
1.00000	-0.22791	-0.22221	-0.08597	-0.08566

APPENDIX B

A brief description for use of the modified code is presented here. It is assumed that the user is familiar with the LTRAN2 program so that only the alterations governing its use will be considered. All user defined input parameters have assigned default values. The code will operate with any number of these redefined by the user as input. In many cases, if default values of some of the parameters are used, the resulting solutions may not have any practical significance. The following list itemizes the user defined parameters:

Variable Name	Variable Type	Default Value	Description
VISC	Logical	FALSE	Defines boundary-layer option FALSE--no viscous calculation TRUE--perform viscous calculation
XOFFST	Real	0.02	Offset of wedge from sonic point, x_o.
XPREC	Real	0.02	Length of wedge precursor, x_p.
XRAMP	Real	0.10	Length of ramp, x_R
IBLCAL	Integer	1	Iteration increment for performing viscous calculation
GREEN	Logical	FALSE	Defines lag entrainment option FALSE--use viscous wedge only TRUE--integrate lag entrainment equations
REYINF	Real	1.0E7	Chord Reynolds number based on freestrem conditions, Re_∞

TINF	Real	300.0	Freestream temperature in degrees Kelvin, T_∞
PRT	Real	0.9	Turbulent Prandtl number, Pr_t (default value is for air)
SO	Real	110.0	Sutherland law viscosity constant in degrees Kelvin, So (default value is for air)
IBLPRT	Integer	50	Iteration increment for printing viscous parameters

The logical variable VISC has been added to the namelist INPUT. If no viscous calculations are desired, VISC may be input as FALSE or the default value taken. This will permit the code to operate in the inviscid mode. If VISC is input as TRUE, it indicates that a viscous computation is to be performed. In addition the program expects to find another namelist of input variables immediately following INPUT. The new namelist name is VCALC. Note that even if no parameters are defined in VCALC, a card of the form $VCALC $ must appear in the input data. Conversely, if VISC is FALSE, the namelist VCALC must not appear.

The remaining parameters are defined in the VCALC namelist. The variables XOFFST, XPREC, and XRAMP are the parameters defining the ramp geometry. In general the optimal choice for these is case dependent, but the default values have proven adequate for a large number of both steady and unsteady computations. IBLCAL is an integer variable available to control how often the viscous displacement is updated. It is suggested that this be done every time step, but for certain applications an alternate procedure may be desirable. GREEN is a logical variable controlling selection of the lag entrainment calculation. If GREEN is FALSE only the viscous wedge is used. With GREEN set to TRUE the lag entrainment equations will be integrated.

When the lag entrainment option is selected, the variables REYINF, TINF, PRT, and SO must be specified. These are the parameters which define the physical flow under consideration. The default values will have no significance in this case. Finally, IBLPRT is an integer variable which determines the number of time steps between printing values of the viscous parameters. This printing gives distributions of

$$\frac{1}{\delta}\ \frac{d\left(\frac{\delta^*}{c}\right)}{d_x}, \frac{\theta}{c}, H, C_E, \text{ and } \frac{\delta^*}{c}$$

along the airfoil and trailing wake for the upper and lower surfaces. Note that no printout occurs for the wedge solutions unless the lag entrainment equations are integrated.

The input for running the code in its various modes is as follows.

1.	Inviscid	The code will run inviscidly by setting VISC = .FALSE., or by using its default value.
2.	Wedge Only	In namelist INPUT set VISC = .TRUE. Namelist VCALC must now appear even if default values are taken. XOFFST, XPREC, XRAMP, AND IBLCAL may be defined or default values taken. All other variables are not needed, but GREEN = .FALSE. if defined. This is also its default value.
3.	Lag Entrainment	Set VISC = .TRUE. in namelist INPUT. In namelist VCALC, set GREEN=.TRUE. Ramp parmeters may be defined or default values taken but REYINF, TINF, PRT, and SO must be defined for the specific flow conditions. Other parameters are user optional.

In order to generate a steady viscous solution, the airfoil surface boundary condition must be augmented by the viscous displacement through an unsteady time integration. This is done by setting the amplitude of the unsteady motion (ALFONE) to zero. Choice of the time step is controlled by input variables XK and NSPC, which will be case dependent. Implementation of the wedge requies that the minimum pressure on the airfoil occur somewhere between the leading and trailing edge. If this situation is characterized by a shock, the wedge will be located within the shock profile. In addition, if the lag entrainment equations are to be solved, they will apply aft of the shock up to the downstream boundary. When no shock occurs, the wedge is not applied, but the lag entrainment solution (if this option is selected) will commence at the point of minimum pressure.

Thus, to obtain the viscous solution the calculation should begin with a well behaved inviscid result as the initial condition. This result need not be converged, but should have the essential features of a converged solution. If it is not possible to obtain a reasonable inviscid result for the given flow conditions, these may be altered until the viscous modifications are implemented. For example, if in the inviscid solution the shock lies at the trailing edge, the Mach number and/or angle of attack may be reduced. This allows the shock to move upstream. Once the inviscid starting solution is obtained, viscous input parameters may be set to their desired values for the computation of the viscous solution. After the steady viscous solution has been generated, it will serve as the initial condition for any unsteady viscous calculation.

1. Report No.	2. Government Accession No.	3. Recipient's Catalog No.
NASA CR-166249		

4. Title and Subtitle	5. Report Date
PROCEDURES FOR THE COMPUTATION OF UNSTEADY TRANSONIC FLOWS INCLUDING VISCOUS EFFECTS	August 1981
	6. Performing Organization Code
7. Author(s)	8. Performing Organization Report No.
Donald P. Rizzetta	
9. Performing Organization Name and Address	10. Work Unit No.
Boeing Military Airplane Company P. O. Box 3707 Seattle, WA 98124	505-31-11
	11. Contract or Grant No.
	NAS2-10762
12. Sponsoring Agency Name and Address	13. Type of Report and Period Covered
National Aeronautics and Space Administration Washington, DC 20546	Contractor Report
	14. Sponsoring Agency Code

15. Supplementary Notes

Ames technical monitor: Peter M. Goorjian
Final Report for Phase I of Contract

16. Abstract

Modifications of the code LTRAN2, developed by Ballhaus and Goorjian, which account for viscous effects in the computation of planar unsteady transonic flows are presented. Two models are considered and their theoretical development and numerical implementation is discussed. Computational examples employing both models are compared with inviscid solutions and with experimental data. A description for use of the modified code is provided.

17. Key Words (Suggested by Author(s))	18. Distribution Statement
Unsteady Transonic Flow Viscous Corrections Code LTRAN2	Unlimited STAR Category - 02

19. Security Classif. (of this report)	20. Security Classif. (of this page)	21. No. of Pages	22. Price*
UNCLASSIFIED	UNCLASSIFIED	73	

*For sale by the National Technical Information Service, Springfield, Virginia 22161

End of Document